JOURNAL OF GEOPHYSICAL RESEARCH, VOL. 111, E01004, doi:10.1029/2005JE002492, 2006

Mapping compositional diversity on the surface of Mars: The Spectral Variance Index

Sara Martínez-Alonso,[1,2] Michael T. Mellon,[1] Bruce C. Kindel,[1,3] and Bruce M. Jakosky[1,4]

Received 12 May 2005; revised 4 October 2005; accepted 10 October 2005; published 17 January 2006.

[1] The advent of high spatial resolution instruments onboard orbiting Mars missions entails the need for identification of critical regions to be analyzed in further detail. We present the Spectral Variance Index (SVI), a method to detect regions of large surface materials diversity compared to the average of the planet. Such diversity may be indicative of significant active and past geological processes, such as hydrothermal activity, chemical and mechanical sedimentation, pyroclastic volcanism, erosion unveiling layering of diverse composition, and weathering, among others. The SVI was derived from statistical analysis of the Mars Global Surveyor Thermal Emission Spectrometer spectral data set for 5 × 5 degree cells covering the entire planet; global SVI maps depicting surface materials diversity were produced. Regions of elevated SVI occur clustered in low-albedo, high-thermal inertia regions, indicative of rock-dominated surfaces. The surface geology of two regions of anomalously high SVI (Nili Fossae and Mare Tyrrhenum), and one region of low SVI (Amazonis Planitia), was investigated utilizing spectroscopic, thermophysical, and morphological data. The following data-derived spectral end-members were identified in all three regions: atmospheric water-ice, surface dust (both in close spatial relationship), and instrument noise. The high SVI regions show also signatures characteristic of surfaces type 1 and 2, forsterite (Nili), phyllosilicates and/or high-Si glass (Nili), and another end-member most consistent with fayalite (or, alternatively, high-Ca pyroxene) in volcanic materials (Tyrrhenum). The SVI method effectively identifies regions, both previously known and new ones, of surface material diversity on Mars; spectroscopic data of higher spatial resolution will improve our understanding of their compositional diversity.

Citation: Martínez-Alonso, S., M. T. Mellon, B. C. Kindel, and B. M. Jakosky (2006), Mapping compositional diversity on the surface of Mars: The Spectral Variance Index, *J. Geophys. Res.*, *111*, E01004, doi:10.1029/2005JE002492.

1. Introduction

[2] Visible and infrared spectrometers of high spatial resolution onboard ongoing and future Mars orbiting missions will allow for detailed surface composition mapping of critical regions in that planet, necessary for the identification of future landing sites. Identifying from existing global data sets such critical regions is essential to optimize the scientific return of those missions. In this study we present a new method developed to identify, from statistical analysis of the Mars Global Surveyor Thermal Emission Spectrometer (MGS-TES) global data set, regions on the surface of Mars characterized by higher than average spectral variance, and therefore dominated by the presence of diverse geological materials, rather than by a spectrally homogeneous cover. The spectral end-members responsible for the variance quantified in critical SVI regions are subsequently extracted from the data themselves and identified. Because a few TES spectra different from the average background signature can increase significantly the regional spectral variance, this extraction method allows for the detection of relatively small outcrops of distinct materials.

[3] Many relevant geological processes result in the concentration of a large diversity of surface materials (minerals, lithologies) in small regions. As an example, terrestrial hydrothermal systems are characterized by the presence of a wide variety of mineral species in relatively small geographical areas; because each mineral species has a distinct spectral signature, this translates into higher than average variance in the spectral remote sensing data of hydrothermal areas [*Boardman and Green*, 2000; *Green and Boardman*, 2000]. Other geological processes that produce/concentrate a large variety of surface materials are: chemical sedimentation (such as water-laid deposition of carbonates and evaporites, characterized by layering of

---

[1] Laboratory for Atmospheric and Space Physics, University of Colorado, Boulder, Colorado, USA.

[2] Now at Department of Geological Sciences, University of Colorado, Boulder, Colorado, USA.

[3] Also at Program in Atmospheric and Oceanic Sciences, University of Colorado, Boulder, Colorado, USA.

[4] Also at Department of Geological Sciences, University of Colorado, Boulder, Colorado, USA.

0148-0227/06/2005JE002492$09.00

diverse composition), clastic sedimentation (such as in glacial and fluvial systems), pyroclastic volcanism, erosion unveiling layering, and differential weathering (chemical, mechanical), among others. Understanding those processes would be of great importance to understanding the geological, hydrological, and, potentially, biological history of Mars: sedimentary deposits and weathering (or lack thereof) would be indicative of past and present climatic and hydrological regimes; hydrothermal and water-laid deposits would be prime sites to look for chemical and biological signatures of past and present life on Mars.

[4] The nature of surface materials (lithology, mineralogy, mineral composition) can be determined from remote sensing spectroscopic data such as those acquired by TES. TES data made possible for the first time the positive identification on the surface of Mars of mineral species such as olivine [*Hoefen et al.*, 2000, 2003; *Hoefen and Clark*, 2001; *Hamilton et al.*, 2001, 2003] and hematite [*Christensen et al.*, 2000a, 2001a]. Other minerals (e.g., plagioclase, high-Ca pyroxene, phyllosilicates and/or high-Si glass, carbonates) were also inferred from TES spectral data [*Bandfield et al.*, 2000; *Christensen et al.*, 2000b, 2001b; *Bandfield*, 2002, 2003; *Bandfield et al.*, 2003]. On the basis of geologic evidence indicating volcanic activity and liquid water available at the surface throughout Martian history, we can expect relict and/or active hydrothermal systems to exist on Mars [*Walter and Des Marais*, 1993]. However, sound mineralogical evidence of hydrothermal systems on Mars has not yet been found, perhaps due to the coarse spatial resolution of the TES spectroscopic data and/or to the use of spectral analysis techniques not aimed to detect small occurrences of distinct mineralogy. (TES is to date the only global spectroscopic data set available with close-to-full coverage of the surface of Mars at 3 × 6 km resolution; terrestrial hydrothermal systems have exposed surfaces commonly on the order of 10–100 km^2, equivalent to 1–6 TES spectra). Likewise, previous investigations based on remote spectroscopic measurements have failed to show exposed water-laid deposits; however, such deposits may exist on Mars: In situ observations of the Mars Exploration Rover (MER) Opportunity, were identified as indicative of the presence of minerals (jarosite) and textures (cross-stratification) which can be found in, among others, terrestrial evaporitic environments [*Squyres et al.*, 2004a]. Hydrated sulfates were also identified in Mars Express OMEGA orbiting data; such deposits may have been produced by mechanisms other than evaporation in long-standing bodies of water, though, such as precipitation from acidic rain or frost alteration of basalts [*Bibring et al.*, 2005].

[5] Most of the previous TES mineralogical studies were based on unconstrained (i.e., negative abundances of minerals are allowed) linear deconvolution of the TES spectral data utilizing laboratory-measured library spectra; this is a well-established technique apt for derivation of quantitative surface mineralogy [*Bandfield et al.*, 2000; *Bandfield*, 2002]. A different approach was utilized by *Hoefen et al.* [2000, 2003] and *Hoefen and Clark* [2001], who applied in their analyses a spectral feature mapping algorithm [*Clark et al.*, 2003] which looks in a library of reference spectra for the best match to the TES data. *Altieri and Bellucci* [2003] analyzed TES spectral data of discrete regions of Mars, based on cross-plotting the second principal component obtained for the 300–550 cm^{-1} and the 815–1143 cm^{-1} TES spectral ranges respectively, and on the goodness of fit between a straight line and the TES spectra in the 300–550 cm^{-1} range.

[6] In this study, an alternative approach is utilized in the analysis of the TES spectral data, based on (1) quantification of the spectral variance of surface materials through the calculation of a global Spectral Variance Index (SVI); (2) focus on regions of high SVI, indicative of larger than average surface-materials diversity; and (3) extraction of the spectral end-members necessary to explain the variance in the nonaveraged (spatially or spectrally) data from the data themselves. This approach has three main advantages: First, it provides a new, complementary global view of the spectral properties of the surface of that planet, indicative of the degree of diversity of exposed materials. Second, it allows for the detection of spectral anomalies caused by a few TES spectra departing from the average, and potentially corresponding to relatively small deposits of distinct materials. Last, the data-derived end-member detection method utilized is not dependent on spectral libraries, which are inherently incomplete.

[7] Following, we describe the SVI methodology and the data utilized in this study, we present the global SVI results, and we analyze in detail three regions selected according to their SVI values. Next, we discuss the significance of the SVI results by comparison to other global surface properties, and to in situ data. From this analysis we conclude that: the SVI method is suitable for the identification of regions of large diversity of surface materials; data-derived end-member extraction allows for the separation of the spectral units present in a data set, independently of spectral libraries; and detection of small occurrences of spectrally distinct materials is possible following the approach described here.

2. Methodology

[8] Since the onset of the MGS mission in 1998, TES has acquired more than 200 million emission spectra covering a large percentage of the total surface of Mars, which is approximately equivalent to the total land surface area on Earth. Analyzing all the information present in the TES data set is a challenging task, due both to the extensive geographic coverage and to the large size of the spectral data set. To identify spectrally critical regions, the SVI method, which quantifies spectral variance per surface unit, was devised.

2.1. TES Spectral Emissivity Data

[9] TES measures spectral radiance in 143 (single-scan mode) or 286 (double-scan mode) bands that span the 148–1715 cm^{-1} range [*Christensen et al.*, 1992, 2001b]; the spatial resolution of each single-scan spectrum is approximately 3 × 6 km. Spectral emissivity is calculated for each spectrum as described by *Christensen et al.* [2001a]. We present results derived from the analysis of publicly available TES single-scan emissivity data available to date

Table 1. Thermal Emission Spectrometer Spectral Data Selection Criteria

Data Selection Criteria	Database Field
Single length scan (no spatial averaging)	scan_len = 1
No detectors averaging	det_mask = 7
No spectral averaging	spectral_mask = 00
Close to nadir view	emission $\leq$ 30
Day data only	incidence $\leq$ 90
Surface temperature	target_temp $\geq$ 250
Low atmospheric dust opacity	nadir_opacity[1] $\leq$ 0.2
Low atmospheric ice opacity	nadir_opacity[2] $\leq$ 0.06
No image motion compensation	pnt_imc = 0
Data quality[a]	atmospheric_opacity_rating = 0 0 spectrometer_noise = 1 1 algor_patch = 1 1 major_phase_inversion = 0 0 algor_risk = 0 0

[a] The high gain antenna motion (hga_motion = 1 1) and solar panel motion (solar_panel_motion = 1 1) fields were not included because they were found to cause the rejection of approximately half of the spectra, most of them corresponding to good quality observations.

(TES orbits since orbit insertion or "ocks" 1583 to 21003) from the mapping and extended missions. TES double-scan emissivity data corresponding to the same orbit range were also utilized to corroborate results obtained in the analysis of the single-scan data.

[10] Prior to the spectral analysis, daytime TES emissivity spectra of the regions of interest were gathered. Data were selected according to several quality criteria (Table 1): no spatial or spectral averaging, close-to-nadir acquisition geometry, low atmospheric dust and water-ice opacities, brightness temperatures equal to or greater than 250 K for maximum signal to noise, and instrument performance. The spectra acquired by each of the 6 TES detectors were resampled to a common set of wave numbers (the average of the six TES detectors) and full-width-half-maxima (to match those of TES detectors 1 and 3, the ones with the lowest spectral resolution). Spectral bands below 223 cm^{-1} and above 1400 cm^{-1} were not included in this analysis because of the higher noise equivalent spectral radiance in these ranges [*Christensen et al.*, 2000b]; bands between 573 and 764 cm^{-1} (the spectral region dominated by atmospheric CO_2 absorption) were also discarded. Noise-dominated spectra characterized by radical excursions from the common emissivity values, sine-like and saw-like patterns, were identified and discarded applying a noise-rejection algorithm that computes the sums of absolute differences in emissivity between adjacent bands in the 255–552 and 1326–1400 cm^{-1} ranges, where most of that noise is. Two empirically derived thresholds (0.25 and 0.20, respectively) were utilized to isolate the noisy spectra (Figure 1); exhaustive visual examination of the accepted and rejected spectra indicates the method and the thresholds are appropriate. The spectra identified by this procedure are consistent with instrument noise (see for example spectra *c* through *i* in Figure 1), as well as with the signature produced by elevated amounts of atmospheric water vapor (compare spectra *a* and *b* shown in Figure 1); the latter will be discussed in the following section. When more than one TES observation that met our quality criteria existed for a single ground instantaneous field of view, the first observation was utilized to minimize instrument-noise of unclear origin, which has grown progressively worse through TES operation [*Bandfield*, 2002]; the expression of this type of noise is a feature near 1000 cm^{-1},

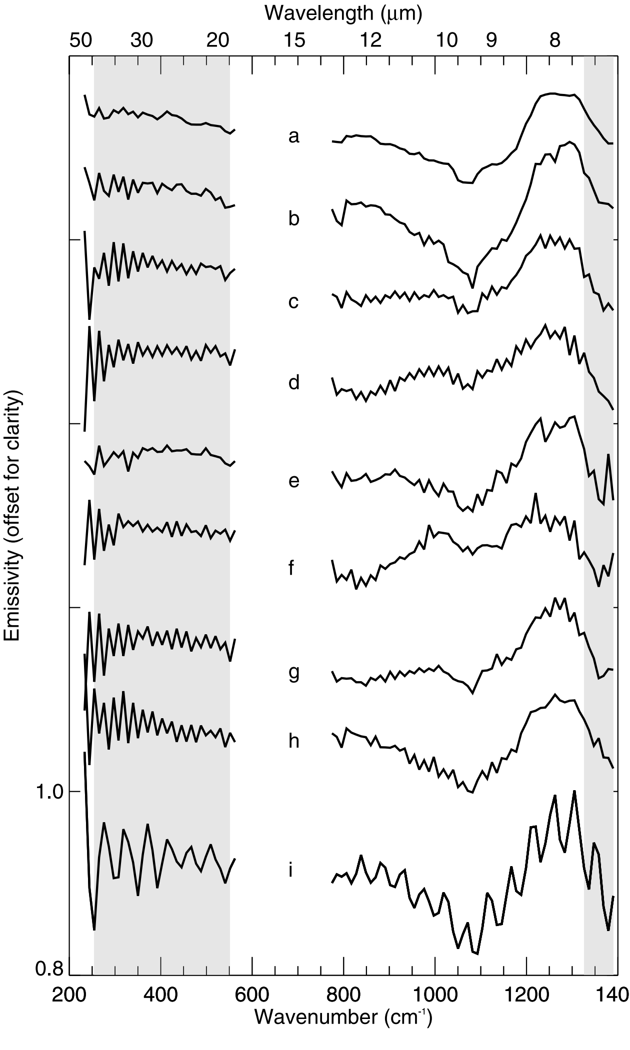

Figure 1. Thermal Emission Spectrometer (TES) emissivity spectra: (a) is an example of nonnoisy data; (b) through (i) represent spectra identified by our noise-rejection algorithm. Spectra (c) through (i) are consistent with instrument noise; spectrum (b) presents the signature characteristic of elevated atmospheric water vapor. Shaded boxes indicate bands utilized to isolate noisy spectra (see text for explanation). No contrast enhancement or scaling was applied to any of the spectra.

contrasting with the sinus-like or saw-like noise described above.

2.2. Atmospheric Contribution to the TES Spectral Emissivity Data

[11] The signature of gases and aerosols in the Martian atmosphere interfere with the surface emissivity in the following spectral regions: CO_2 mostly near 667 cm^{-1}, minor effects near 550, 790, 961, 1064, 1260, and 1366 cm^{-1}; H_2O vapor in the 200–400 and 1400–1800 cm^{-1} regions; dust near 1075 cm^{-1}; H_2O ice near 825, 229 cm^{-1} [*Smith et al.*, 2000a].

[12] Available atmospheric correction models capable of performing spectrum-by-spectrum surface-atmosphere separation such as the deconvolution method described by *Smith et al.* [2000a] require a priori assumptions on the composition of the Martian surface and depend on the spectral libraries utilized. Other atmospheric correction methods, such as the one described by *Bandfield and Smith* [2003], based on a correlated-k band model [*Goody et al.*, 1989] and derived from the line-by-line spectral database GEISA-97 [*Husson et al.*, 1992, 1994], are appropriate to remove minor CO_2 bands and water vapor absorption effects without a priori assumptions about surface composition; however, their elevated computational cost makes them impractical when analyzing very large data sets, such as in the global SVI calculation. (Also, full application of the multiangle Emission Phase Function (EPF) method of *Bandfield and Smith* [2003] requires multiple angle emission angle observations only available for a very small number of locations). For these reasons, a full atmospheric correction was not performed, opting instead for minimizing the atmospheric effects in the data by rejecting data with high atmospheric dust, water-ice, and water vapor opacities; the strong CO_2 band near 667 cm^{-1} impedes the study of surface emissivity in that spectral region even after a full atmospheric correction. Data affected by elevated atmospheric dust and water-ice were rejected according to opacity values derived on a spectrum-by-spectrum basis as described by *Smith et al.* [2000b] and *Pearl et al.* [2001], respectively. As indicated previously, our algorithm for noise rejection also filters out spectra with a strong atmospheric water vapor component. The spectrum of water vapor in the 200–400 cm^{-1} range convolved to the TES spectral resolution presents a characteristic "picket-fence" appearance [*Smith*, 2002], resulting in high values for our noise-rejection algorithm computed in the 255–552 cm^{-1} range. The spatial distribution of percentage of rejected spectra per cell (Figure 2a) shows a remarkably well organized spatial distribution, very similar to that of atmospheric water vapor abundance (Figure 2b), and topography (Figure 2c). We assume that the rejected spectra corresponding to instrument noise have a mostly random spatial distribution; therefore the spatial distribution observed in Figure 2a is interpreted as dominated by atmospheric water vapor abundance, which is itself strongly anticorrelated with topography [*Smith*, 2002].

2.3. Other Data Sets Utilized

[13] The geological significance of regions selected according to their SVI values was investigated utilizing a comprehensive approach, analyzing, besides the TES spectral data, other public remote sensing data sets available for those regions: thermal inertia and albedo values, visible and infrared imagery, as well as topographic data.

[14] Thermal inertia and albedo values were utilized to characterize the thermophysical properties of surface materials (e.g., particle size, rock/bedrock exposure, and degree of induration); those properties constrain the physical character of the surface and the geological context of the materials identified in the spectral analysis. Thermal inertia values were derived from TES nighttime bolometric brightness temperatures utilizing the model described by *Mellon et al.* [2000]. TES-derived albedo values [*Christensen et al.*, 2001b] were analyzed to determine the spatial distribution of bright and dark surfaces, indicative of dust coverage. Thermal inertia and albedo values were filtered to avoid periods of high atmospheric opacity: infrared opacity threshold values of 0.20 and 0.06 were utilized for dust and water-ice opacity, respectively. To facilitate their interpretation, the thermophysical properties of the regions of interest were analyzed in comparison to the global thermophysical units defined by *Mellon et al.* [2000] and *Putzig et al.* [2005] (Figure 3), and subsequently mapped back into the spatial domain to analyze their areal distribution and spectral and morphological characteristics.

[15] High spatial resolution morphological data were analyzed to understand the geological context of the materials identified in the analysis of the spectral and thermophysical data: MGS-Mars Observer Camera (MOC) [*Malin et al.*, 1992] and Mars Odyssey THEMIS [*Christensen et al.*, 2003, 2004] imagery, as well as MGS-Mars Observer Laser Altimeter (MOLA) topographic data [*Zuber et al.*, 1992].

[16] To facilitate their joint analysis, all these data sets were rectified to fit the simple cylindrical projection and areocentric coordinate system as defined in the IAU2000 report [*Seidelmann et al.*, 2002]. Longitudes are given in degrees west of the prime meridian and all figures are oriented with north up.

2.4. Spectral Variance Index (SVI) Method

[17] To identify areas on Mars spectrally dominated by the presence of a variety of surface materials (minerals, lithologies) rather than by an homogeneous cover, a global SVI map was derived from statistical analysis of the TES spectral single-scan data set [*Martínez-Alonso*, 2002; *Martínez-Alonso et al.*, 2002, 2003]. The SVI quantifies the amount of spectral variance in the TES emissivity data per surface area. The spectral variance per band measures, in a set of spectra, the average departure in emissivity from the band's mean:

$$\mathrm{var}_k = \frac{\sum_{i=1}^{n} (\varepsilon_{ik} - \mu_k)^2}{n - 1} \qquad (1)$$

var_k	spectral variance for band k.
n	number of spectra in the set considered.
ε	emissivity.
μ	mean emissivity.

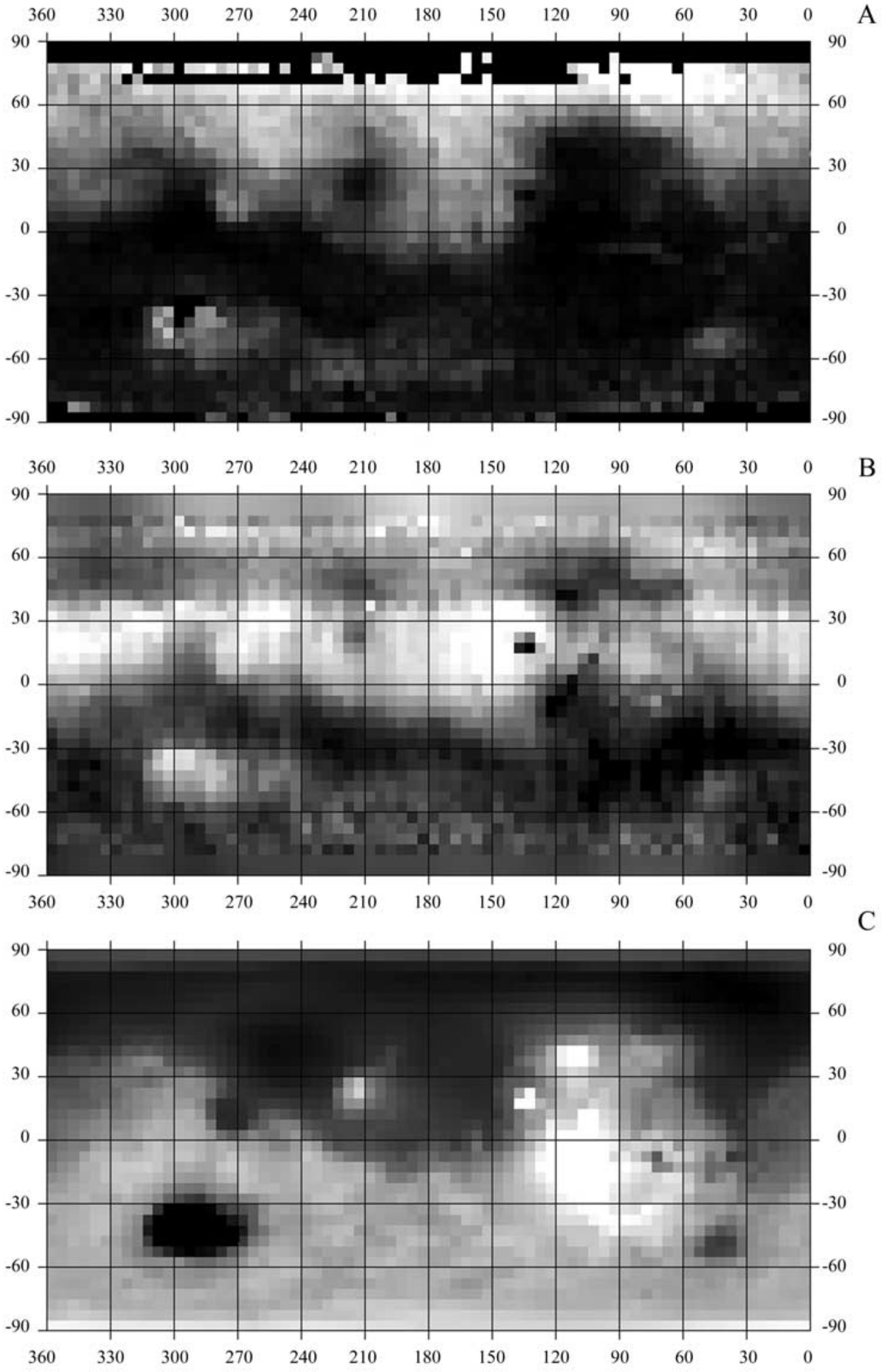

Figure 2. (a) Spatial distribution of percentage of spectra identified and discarded according to our noise-rejection algorithm; lighter tones of gray indicate higher percentages. The algorithm discards data with a spectral signature consistent with instrument noise and with that produced by elevated amounts of atmospheric water vapor (see text for details). (b) Atmospheric water vapor not normalized for atmospheric pressure, strongly anticorrelated with topography; lighter tones of gray indicate higher abundances (data from *Smith* [2002]). (c) MOLA topography; lighter tones of gray indicate higher elevation; data was subsampled to match the spatial resolution of the other two panels.

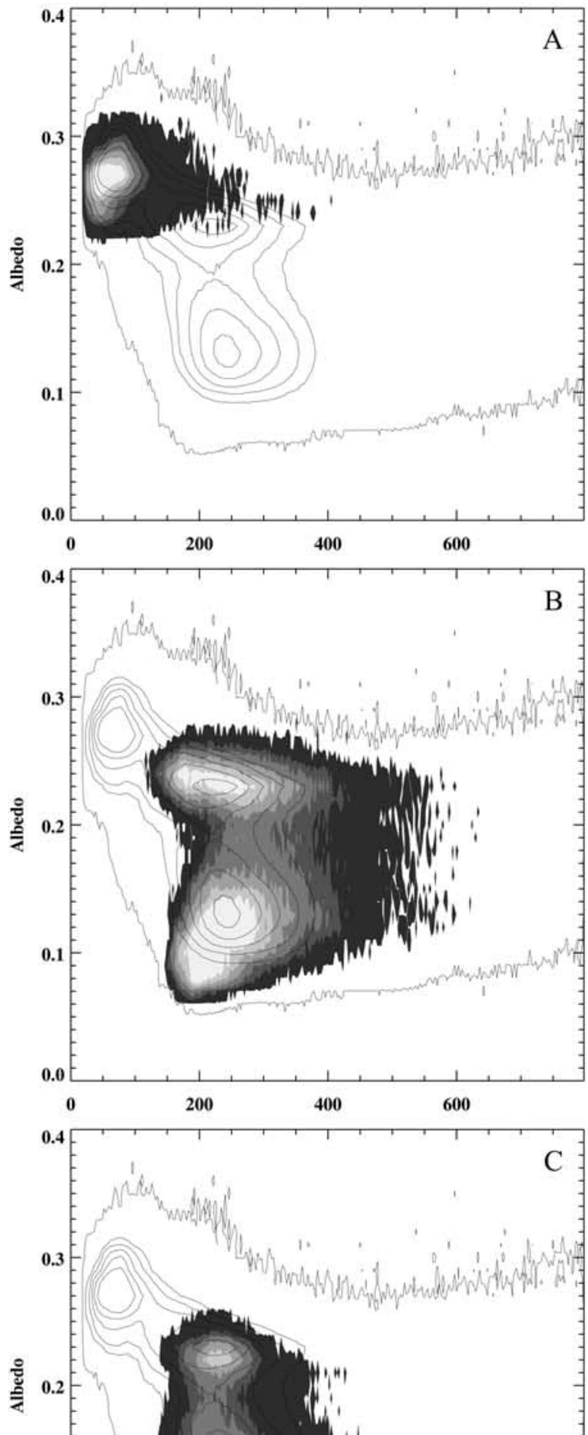

[18] The total spectral variance is the sum of the variances calculated for each of the spectral bands considered, and is equal to the sum of their eigenvalues. If all the spectra in the data set have similar emissivity properties, both in the location and amplitude of their minima and maxima (that is, if all the spectra correspond to the same material), then their spectral variance will be low. Conversely, if the data set considered is constituted by different types of spectra (different materials), its spectral variance will be higher.

[19] The process followed to calculate the global SVI values is summarized in Figure 4. First, all available daytime TES emissivity single-scan spectra were collected for 5 × 5 degree cells (approximately 90,000 km^2) covering the entire planet, and filtered as described in section 2.1. Spectral bands in both the 223–573 cm^{-1} and 764–1400 cm^{-1} ranges were utilized in the global SVI calculation; the calculation was repeated for each of these two spectral ranges separately to evaluate the atmospheric contribution to the SVI results. To obtain the SVI, the TES emissivity spectra gathered for each cell were first processed applying the Minimum Noise Fraction (MNF) transformation [*Green et al.*, 1988; *Boardman and Kruse*, 1994]. The MNF transformation is used to segregate noise from the data and to reduce the computational requirements for subsequent processing. It consists of two cascaded principal components transformations: the first one decorrelates and rescales the noise in the data (the noise thereafter has unit variance and no band-to-band correlations); the second transformation is a standard principal components transformation of the noise-adjusted data. The noise covariance matrix was calculated from shift differences of half a million TES internal black body emissivity spectra, which were collected at regular intervals during the normal operation of the sensor. The shift difference technique, based on the minimum/maximum autocorrelation factors procedure developed by *Switzer and Green* [1984], assumes that "adjacent" spectra contain strongly correlated signal, while their noise component is only weakly correlated. The spectral variance per cell was computed by summing the resulting noise-adjusted MNF eigenvalues, which are above 3 standard deviations of the noise.

[20] As expected, there is some correlation between spectral variance and number of spectra per cell (Figure 5); the linear regression between both parameters was calculated

Figure 3. Two-dimensional histograms of TES albedo versus TES-derived thermal inertia for the study areas: (a) Amazonis Planitia, (b) Nili Fossae, and (c) Mare Tyrrhenum. Frequencies of occurrence are shown in shades of gray; lighter gray levels indicate higher frequencies. Mars global values are shown in each panel by black contour lines; the three modes of frequent correlation in the global values were interpreted by *Mellon et al.* [2000] as follows: "global unit A", of low thermal inertia and high albedo, dominated by bright, fine-grained, unconsolidated materials; "global unit B", with high thermal inertia and low albedo, dominated by coarse materials (sand, rocks, bedrock) and some duricrust; and "global unit C", of moderate to high thermal inertia and intermediate albedo, corresponding to indurated materials with some sand, rocks, and bedrock.

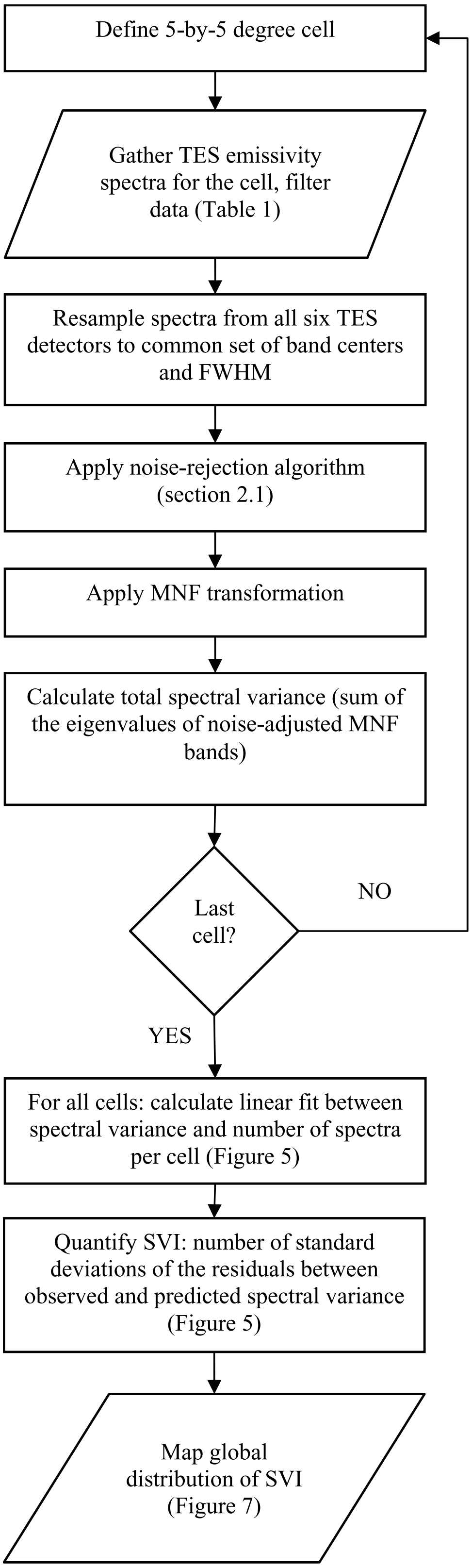

Figure 4. Flowchart summarizing the procedure followed in the SVI calculation.

utilizing a robust least absolute deviation technique [*Press et al.*, 1992]. However, the uneven scatter observed in Figure 5, noticeably more prominent above the linear fit than below it, and the significant but less than perfect R^2 value of the regression (0.30) indicate that the spectral variance in the data is not a function of the number of spectra alone and that some cells are indeed spectrally more complex than the average. The SVI quantifies the departure from that linear fit, and is expressed as the number of standard deviations of the residuals between observed and predicted (from the regression) spectral variance per cell. SVI values range between −3.49 and 10.29, with a mean of 0.18 and a standard deviation value of ±1.61 (Table 2). Cells whose observed spectral variance is at least three standard deviations above its predicted value (SVI $\geq$ 3) are considered anomalously high.

[21] To demonstrate the performance of the SVI, two sensitivity analysis tests were carried out. From the global SVI map, a control cell with an average number of TES spectra (5915) and SVI close to 0 was selected. Detailed

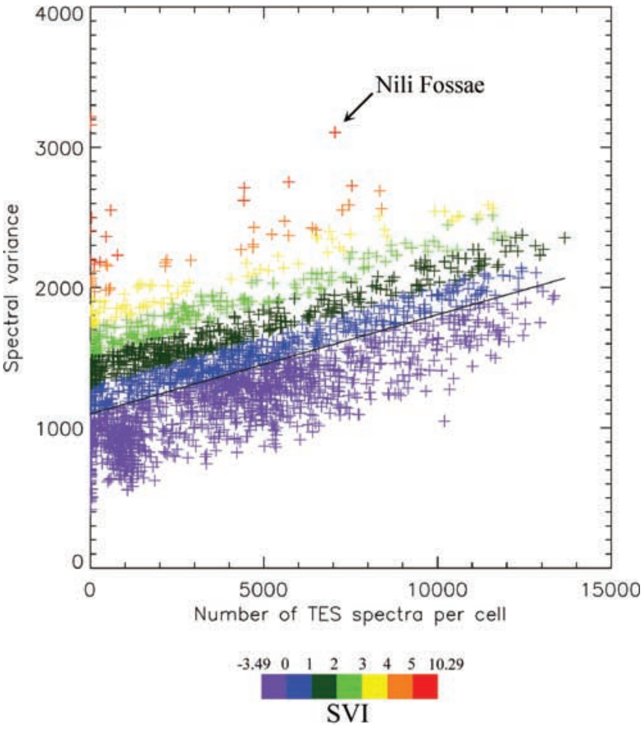

Figure 5. Distribution of total spectral variance derived from the 233–562 and 775–1400 cm^{-1} ranges versus number of TES emissivity spectra per cell. Each data point (cross) corresponds to a single 5 × 5 degree cell. As expected, there is some correlation between spectral variance and number of spectra per cell; the black line represents the linear regression fitted to the data. The Spectral Variance Index (SVI) is expressed as the number of standard deviations of the residuals between observed and predicted (from the regression) spectral variance per cell. Colors show intervals of SVI values. High SVI values are indicative of large diversity of surface materials, compared to the average of the planet. Label identifies one of the high SVI cells, in the Nili Fossae region, of previously recognized mineralogical/lithological diversity.

Table 2. Statistics of the Spectral Variance Index Values for the Global Distribution and for Each of the Three Study Regions[a]

Location	Coordinates	SVI Values Average (±stdv)	Minimum	Maximum
Global distribution	-	0.18 (±1.61)	−3.49	10.29
Amazonis Planitia	30°N 180°W, 0°N 150°W	−1.36 (±1.02)	−3.16	0.89
Nili Fossae	30°N 300°W, 10°N 280°W	2.81 (±1.81)	0.46	7.27
Tyrrhenum Planitia	5°S 240°W, 25°S 220°W	2.55 (±1.32)	0.42	5.08
Viking Lander 1	22.5°N, 48°W	−1.2	-	-
Viking Lander 2	48°N, 225.7°W	0.5	-	-
Pathfinder	19.3°N, 33.5°W	−0.4	-	-
MER Spirit	14.6°S, 184.5°W	−0.3	-	-
MER Opportunity	1.9°S, 5.5°W	2.7	-	-

[a] The SVI values of the 5 × 5 degree cell containing the five landing sites are also shown, for reference. SVI values were derived from the 233–562 and 775–1400 cm^{-1} ranges.

analysis of the spectral data indicates that, at TES resolution, this 5 × 5 degree cell (centered at 22.5°N, 92.5°W) is dominated by the signatures of surface dust and atmospheric water-ice. A similar number of TES hematite spectra were extracted from the Sinus Meridiani region. The SVI of the original control cell was calculated. Then, 10 of its original TES spectra were substituted by TES hematite spectra, and the SVI of the modified cell was recalculated. This was repeated until all the original TES spectra in the control cell were substituted by TES hematite spectra. A steady increase in variance occurs until more than half of the spectra in the cell were substituted, then the variance remains constant and finally starts to decrease (Figure 6); spectral variance corresponding to SVI = 3 was reached after 35% of the spectra in the control cell were substituted.

[22] In the second test, the original TES spectra in the control cell were substituted one at a time by individual laboratory spectra [*Christensen et al.*, 2000c] of different mineral species common in hydrothermal and magmatic environments; the laboratory spectra were convolved to the TES single-scan bandpass as well as linearly mixed with dust and CO_2 spectra, in order to make them as close to the TES spectra as possible. The SVI of the control cell was recalculated after each substitution. The increase in variance in this case is much more dramatic than in the previous test, reaching that corresponding to SVI = 3 after 0.5% of the spectra in the control cell were substituted (Figure 6).

[23] The first test mimics what can be observed in the Sinus Meridiani region: a large number of spectra of one type of material differing from the background increases significantly the variance in the cell, and therefore its SVI. The second test indicates that a few pure spectra corresponding to a variety of minerals dramatically increases the variance in the cell, leading to anomalously high SVI values.

2.5. Spectral Properties Analysis

[24] The end-members necessary to explain the variance in the TES spectral data of selected study areas were extracted from the data themselves. The purest spectra or end-members in the TES data sets (those that cannot be explained by linear combinations of other spectra in the data set) were extracted utilizing the Pixel Purity Index technique [*Boardman et al.*, 1995], an iterative process consisting of projecting n-dimensional (n being the number of spectral bands considered) scatterplots of the data set onto a random unit vector. The extreme spectra in each projection and the total number of times each spectrum is marked as extreme is recorded; the purest spectra (that is, the data-derived end-members) are recorded the most times. In order to accept that an end-member has spectral significance, repeated observations (performed at different times, either for the same location or for adjacent locations) are always required. Once the spectral end-members were extracted, they were analyzed utilizing constrained (i.e., only positive weights or abundances are allowed) linear mixing models; Last, they were identified by comparison to public spectral libraries [*Jet Propulsion Laboratory*, 2000; *Christensen et al.*, 2000c] and to results from previous studies [*Bandfield et al.*, 2000; *Smith et al.*, 2000a]. To produce surface composition maps, the spatial distribution of the closest matches to the spectral end-members was established applying the Spectral Angle Mapper algorithm [*Kruse et al.*, 1993]. This technique determines the similarity between two spectra (unknown and reference) by calcu-

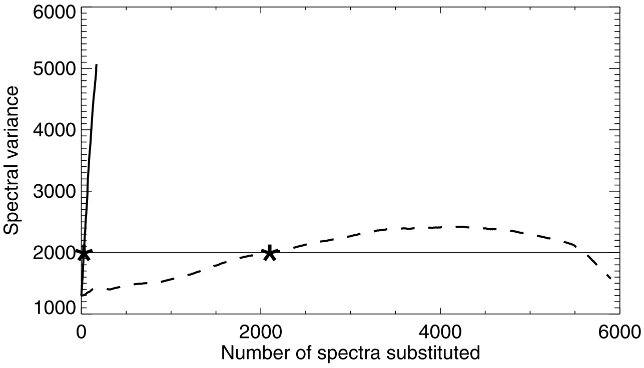

Figure 6. SVI sensitivity analysis results. The original TES data in a 5 × 5 degree cell of average number of spectra and SVI were substituted by TES hematite spectra extracted from Sinus Meridiani (dashed line) and by diverse minerals from a spectral library (solid line). In the first case, SVI = 3 is reached after 35% substitution (asterisk). In the second case, a few spectra of a variety of minerals dramatically increase the spectral variance in the cell, and hence its SVI; SVI = 3 is reached after 0.5% substitution (asterisk). Horizontal line indicates SVI = 3, spectral variance values above this line correspond to higher SVI values.

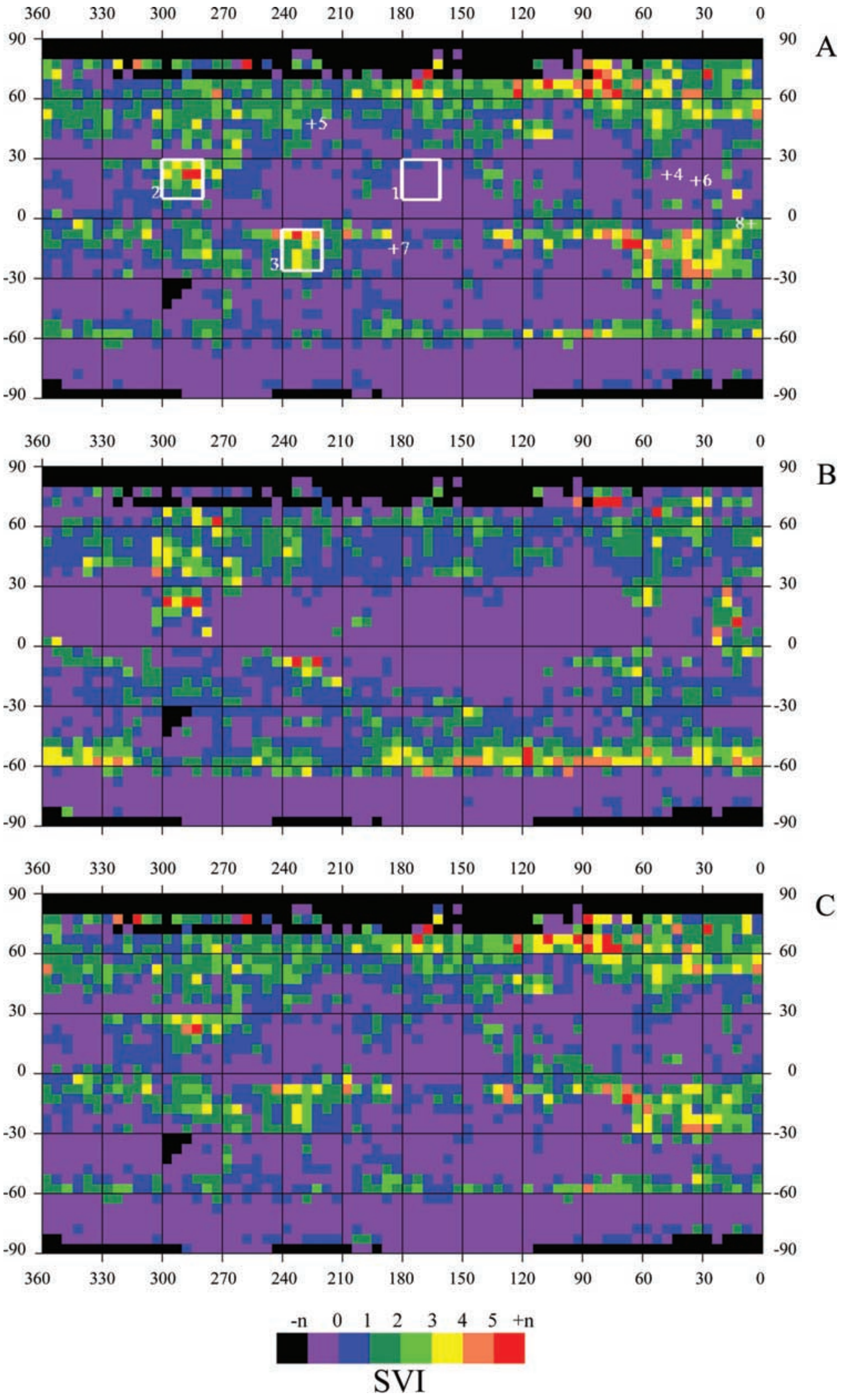

Figure 7. (a) SVI map derived from TES spectral range 1 + 2 (233 to 562 cm^{-1} and 775 to 1400 cm^{-1}); the three study regions and five landing sites are shown for reference: 1, Amazonis Planitia; 2, Nili Fossae; 3, Mare Tyrrhenum; 4, Viking Lander 1; 5, Viking Lander 2; 6, Mars Pathfinder; 7, MER Spirit; 8, MER Opportunity. (b) SVI map derived for spectral range 1 (233 to 562 cm^{-1}). (c) SVI map derived for spectral range 2 (775 to 1400 cm^{-1}). Colors show intervals of SVI values; black indicates lack of data.

Table 3. Spectral Classes Identified in the Amazonis Planitia Region and Their Thermophysical Properties

TES Spectral Class	TES Albedo[a]	TES Thermal Inertia,[a] J m^{-2} K^{-1} s$^{-1/2}$	Thermophysical Global Unit[b]
Dust	0.22–0.32 (0.27 ± 0.01)	24–236 (79 ± 26)	A: unconsolidated fine materials C: duricrust, with some sand, rocks, and bedrock
	0.22–0.31 (0.25 ± 0.01)	190–391 (250 ± 42)	C
Surface type 1[c]	0.12–0.24 (0.19 ± 0.04)	124–376 (224 ± 53)	B: sand, rocks, and bedrock with some duricrust
Water-ice aerosols	-	-	-
Instrument noise	-	-	-

[a] Albedo and thermal inertia given as follows: minimum − maximum (average ± standard deviation).
[b] Defined by *Mellon et al.* [2000] and *Putzig et al.* [2005].
[c] Defined by *Bandfield et al.* [2000].

lating the angle between them, treating them as vectors in the n-dimensional space; smaller angles represent closer matches to the reference spectra (the TES-derived end-members). Spectral end-member mapping was refined in one occasion by utilizing a spectral index that quantifies the depth of a critical absorption band (section 3.4).

3. Results

[25] We present the SVI maps (Figure 7) generated in this investigation as well as initial results obtained in the thermophysical, spectroscopic, and morphological analyses carried out for three regions selected according to their SVI values (Figure 7a): Amazonis Planitia, representative of low SVI regions, as well as Nili Fossae and Mare Tyrrhenum, two high SVI regions. Relevant data for these study areas are summarized in Tables 3, 4, and 5.

3.1. Global Spectral Variance Index Maps

[26] Three global SVI maps were derived: the first map was obtained from the spectral bands in the 223–573 cm^{-1} and 764–1400 cm^{-1} ranges (Figure 7a; hereafter referred to as range 1+2), the other two maps from each of those ranges separately (Figures 7b and 7c; hereafter referred to as range 1 and range 2, respectively). Range 1 is only affected by atmospheric water vapor bands. By contrast, range 2 contains bands corresponding to atmospheric water-ice, CO$_2$, and dust, lacking atmospheric water vapor bands. Given that each of those ranges is affected by different atmospheric components, comparison of the three SVI maps allows for an indirect estimate of the atmospheric contribution to the spectral variance measured by this index.

[27] The three SVI maps have remarkable spatial coherence: high and low SVI values are organized in clusters, rather than being randomly interspersed or mixed in a salt and pepper fashion. In addition, the SVI values show regional gradations, much like elevation or any other trend-surface does; this is equally true in regions of negative SVI. The three SVI maps show the same overall spatial distribution of high and low values, and significant positive correlation among them (Figure 8). Cells of anomalously high SVI value ($\geq$3) occur clustered in discrete geographic locations of low-albedo and high-thermal inertia values, such as in Nili Fossae, Valles Marineris, and Mare Tyrrhenum, as well as along latitudinal bands near 60°N and 60°S. Cells of lower SVI values ($\leq$2) also occur spatially grouped in high-albedo, low-thermal inertia areas such as Arabia Terra, and Amazonis Planitia, among others. The SVI map derived from ranges 1+2 and that derived from range 2 alone are remarkably similar (Figure 8c). This can be explained by the fact that range 2 (59 spectral bands) accounts for more than 80% of the total spectral variance in range 1+2, while range 1 (32 spectral bands) accounts for less than 20%. The three SVI maps showing the same general trends is consistent with the SVI values being mostly driven by surface variance and not by atmospheric effects. Let us further discuss this point by comparing the SVI values obtained from range 1 and range 2 with the variability through time of the main relevant atmospheric components: water vapor, water-ice, dust, and CO$_2$. Because CO$_2$ constitutes more than 95% of the atmosphere and is a well-mixed gas, its variability can be approximated to that of the atmospheric surface pressure.

[28] Dust and water-ice opacity as well as surface pressure values corresponding to the emissivity data utilized in the SVI calculation were obtained from the TES data set; their standard deviation values were calculated for each 5 × 5 degree cell. Maps representing absolute

Table 4. Spectral Classes Identified in the Nili Fossae Region and Their Thermophysical Properties

TES Spectral Class	TES Albedo[a]	TES Thermal Inertia,[a] J m^{-2} K^{-1} s$^{-1/2}$	Thermophysical Global Unit[b]
Dust	0.19–0.29 (0.23 ± 0.02)	118–386 (283 ± 56)	C: duricrust with some sand, rocks, and bedrock
Surface type 1[c]	0.07–0.19 (0.13 ± 0.03)	147–386 (261 ± 51)	B: sand, rocks, and bedrock with some duricrust
	0.09–0.29 (0.19 ± 0.04)	386–780 (451 ± 63)	F: rocks, bedrock, and duricrust
Surface type 2[c]	0.07–0.19 (0.13 ± 0.03)	147–386 (261 ± 51)	B: sand, rocks, and bedrock with some duricrust
	0.09–0.29 (0.19 ± 0.04)	386–780 (451 ± 63)	F: rocks, bedrock, and duricrust
Olivine	0.09–0.29 (0.19 ± 0.04)	386–780 (451 ± 63)	F: rocks, bedrock, and duricrust
Water-ice aerosols	-	-	-
Instrument noise	-	-	-

[a] Albedo and thermal inertia given as follows: minimum − maximum (average ± standard deviation).
[b] Defined by *Mellon et al.* [2000] and *Putzig et al.* [2005].
[c] Defined by *Bandfield et al.* [2000].

Table 5. Spectral Classes Identified in the Tyrrhenum Planitia Region and Their Thermophysical Properties

TES Spectral Class	TES Albedo[a]	TES Thermal Inertia[a] $J\ m^{-2}\ K^{-1}\ s^{-1/2}$	Thermophysical Global Unit[b]
Dust	0.19–0.26 (0.22 ± 0.01)	133–330 (231 ± 31)	C: duricrust with some sand, rocks, and bedrock
Surface type 1[c]	0.10–0.19 (0.13 ± 0.02)	160–355 (248 ± 38)	B: sand, rocks, and bedrock, with some duricrust
	0.09–0.22 (0.11 ± 0.05)	386–723 (414 ± 28)	F: rocks, bedrock, and duricrust
"Undetermined"	0.10–0.19 (0.13 ± 0.02)	160–355 (248 ± 38)	B: sand, rocks, and bedrock, with some duricrust
	0.09–0.22 (0.11 ± 0.05)	386–723 (414 ± 28)	F: rocks, bedrock, and duricrust
Surface type 2[c]?	0.10–0.19 (0.13 ± 0.02)	160–355 (248 ± 38)	B: sand, rocks, and bedrock, with some duricrust
	0.09–0.22 (0.11 ± 0.05)	386–723 (414 ± 28)	F: rocks, bedrock, and duricrust
Water-ice aerosols	-	-	-
Instrument noise	-	-	-

[a] Albedo and thermal inertia given as follows: minimum – maximum (average ± standard deviation).
[b] Defined by *Mellon et al.* [2000] and *Putzig et al.* [2005].
[c] Defined by *Bandfield et al.* [2000].

interseasonal differences in water vapor were produced from atmospheric water vapor column abundances derived by *Smith* [2004] for L_s 105 through 125 (northern summer maximum) and L_s 285 through 305 (northern winter maximum) for Mars years 24 and 25. (According to the nomenclature proposed by *Clancy et al.* [2000], Mars year 1 begins on 11 April 1955; years 24 and 25 begin on 14 July 1998 and 31 May 2000, respectively). Water vapor abundances were derived near the subsolar latitude and therefore do not cover the full latitudinal range. The general trends in water vapor interseasonal differences are analogous for both years; here we discuss results derived for Mars year 24.

[29] Comparison between the SVI maps (Figure 7) and the maps depicting atmospheric components variability (Figure 9) demonstrate the absence of strong spatial correspondence between the two sets of parameters; their two-dimensional histograms (Figure 10) illustrate the poor correlation. The lack of correlation is specially evident for intermediate and high SVI values ($\geq$2); in those cases surface variance supersedes any possible atmospheric effects. The lowest SVI values do show in some cases a slight trend that may be related to atmospheric effects; this is consistent with an atmospheric variance component contributing noticeably to the total spectral variance because the surface variance component is negligible. Local differences among the three SVI maps may be due to the presence of materials with distinct characteristic features in each of the spectral ranges analyzed. In the following sections we will refer to SVI values computed for range 1 + 2.

3.2. Analysis of the Amazonis Planitia Region

[30] This region has low SVI values throughout (Table 2) and was selected to corroborate that low SVI values are indicative of low diversity of surface materials. Amazonis Planitia has been described as smoother than any other large-scale surface observed on Mars [*Aharonson et al.*, 1998]. It is located between the Tharsis and Elysium volcanic provinces, and according to previous studies [*Plescia*, 1990; *Scott and Chapman*, 1991; *Fuller and Head*, 2002] the region resulted from a mixture of fluvial activity and low-viscosity volcanic flooding events, probably of basaltic composition [*Plescia*, 1990; *Keszthelyi et al.*, 2000].

[31] Figures 11a and 11b show TES-derived thermal inertia and albedo maps for the Amazonis Planitia study area. According to them, three thermophysical units, interpreted as dominated by unconsolidated fine materials, duricrust, and rocks, respectively, were identified (Figure 11c) and mapped back into the spatial domain (Figure 11d). Their albedo and thermal inertia properties, as well as their correspondence to the global units defined by *Mellon et al.* [2000] and *Putzig et al.* [2005] are summarized in Table 3.

[32] Analysis of the TES emissivity data shows the presence of four spectral end-members (Figure 11e and

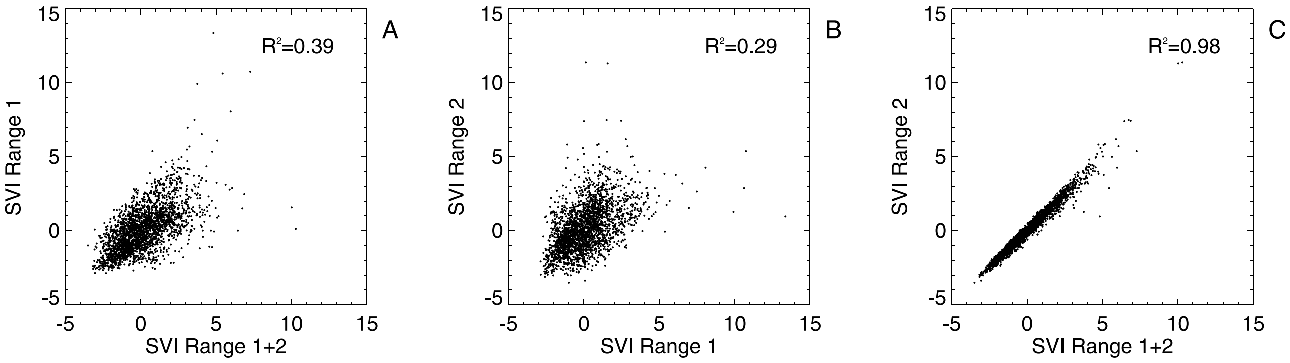

Figure 8. Two-dimensional histograms illustrating the correlation between the global SVI maps derived from each of the three TES spectral ranges analyzed. (a) SVI from range 1 (233 to 562 cm^{-1}) versus that from range 1 + 2 (233 to 562 cm^{-1} and 775 to 1400 cm^{-1}). (b) SVI from range 2 (775 to 1400 cm^{-1}) versus that from range 1. (c) SVI from range 2 versus that from range 1 + 2. Goodness of fit of the regressions (R^2) are indicated for reference.

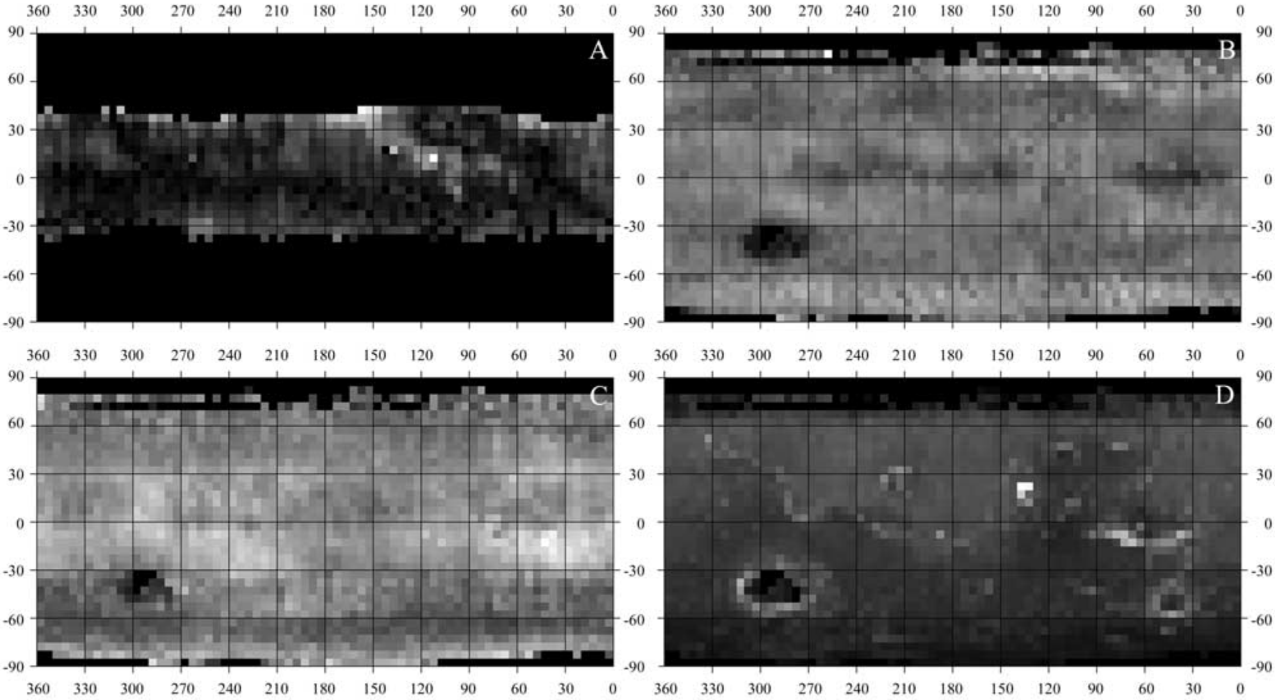

Figure 9. Spatial distribution of the variability through time of relevant atmospheric components (see text for details). Lighter gray levels indicate larger variability values, black indicates lack of data; gray levels were stretched to emphasize subtle differences. (a) Interseasonal differences in atmospheric water vapor between the northern summer and winter maxima for Mars year 24; their mean is 5.803, their standard deviation 4.833; water vapor abundances [from *Smith*, 2004] were derived for subsolar latitude and therefore do not cover the full latitudinal range. (b) Standard deviation of atmospheric dust opacity values; its mean is 0.036, its standard deviation 0.008. (c) Standard deviation of atmospheric water ice opacity values; its mean is 0.011, its standard deviation 0.003. (d) Standard deviation of surface pressure, equivalent to atmospheric CO_2 variability; its mean is 0.43, its standard deviation 0.19.

Table 3) identified as: dust, surface type 1 (commonly interpreted as material of basaltic composition [*Bandfield et al.*, 2000]), airborne water-ice aerosols, and noise. Their spatial distribution is shown in Figure 11f. The water-ice unit is located mostly within a few single TES orbital ground tracks, indicating the atmospheric character of this class. The noise end-member is consistent with noise described by *Bandfield* [2002].

[33] The spectral unit interpreted as dust predominates in the study area; according to thermophysical evidence, it consists mostly of deposits of unconsolidated fine materials, with some discrete regions dominated by duricrust. The thermal inertia values of the unconsolidated materials [*Kieffer et al.*, 1973; *Jakosky*, 1986; *Presley and Christensen*, 1997] indicate their grain size ranges between 0.02 and 300 μm (mean 3 μm), corresponding to clay-to-medium-sand particles, mostly movable by wind. Two significant duricrust-dominated outcrops occur in the study area: one is inside and next to Pettit Crater (12.33°N, 173.78°W), the other in a region centered at 12°N, 159.86°W. The first of these outcrops presents a preferred NE-SW orientation, and coincides with the long-observed Pettit wind streak [*Peterfreund*, 1981; *Pelkey et al.*, 2001]. The second coincides with a region of well-developed yardangs (Figure 12a), oriented NW-SE. The preferential orientation of both outcrops and their thermal inertia relatively higher than that of their surroundings, are consistent with wind denudation of fine materials.

[34] The thermophysical properties of the surface type 1 regions indicate they are dominated by sand, rocks, and bedrock. They account for less than 0.1% of the total surface analyzed, and are localized exclusively in close spatial association with two impact craters: Pettit crater (12.39°N, 173.78°W), and another unnamed crater centered at 15.47°N, 178.39°W. *Rogers and Christensen* [2003] had previously reported a mixture of basaltic and andesitic materials in Pettit Crater; possible scenarios proposed by those authors to account for the presence of basaltic materials in this region of the Northern lowlands are: erosion and deposition of basaltic materials originated elsewhere, excavation due to the impact that produced Pettit Crater, and local basaltic flows. MOC high-resolution imagery of the two regions where we identified the TES basaltic signature (Figures 12b and 12b, respectively) show in both cases the presence of dunes, supporting the first hypothesis. The basaltic dunes in the unnamed crater are circumscribed by rectilinear, graben-like depressions that suggest subsurface collapse.

3.3. Analysis of the Nili Fossae Region

[35] The Nili Fossae region presents some of the highest SVI values in the planet (Table 2). The geology of this

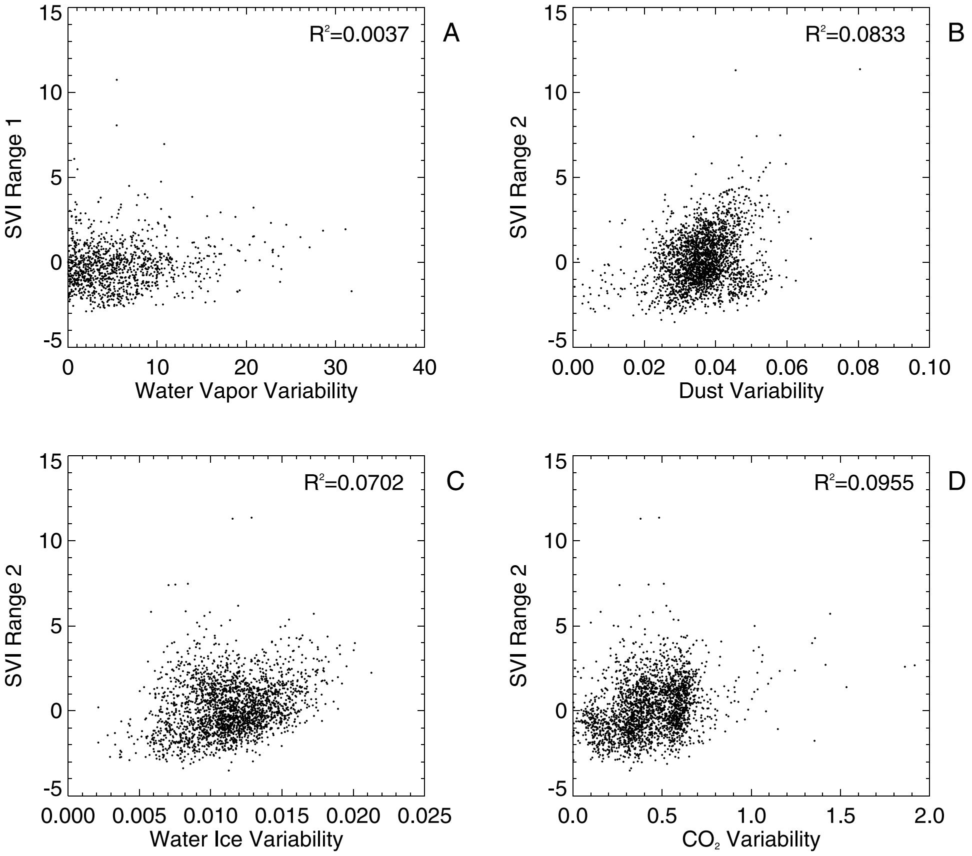

Figure 10. Two-dimensional histograms illustrating the lack of correlation between SVI and variability of relevant atmospheric components, each point corresponds to a 5 × 5 degree cell (see text for details); goodness of fit of the corresponding linear regression (R^2) is shown for reference. (a) SVI values derived from range 1 versus interseasonal differences in atmospheric water vapor for Mars year 24. (b) SVI derived from range 2 versus the standard deviation of atmospheric dust opacity. (c) SVI derived from range 2 versus the standard deviation of atmospheric water-ice opacity. (d) SVI derived from range 2 versus the standard deviation of surface pressure, equivalent to atmospheric CO_2 variability. The lack of correlation is especially evident for intermediate and high SVI values (≥ 2); in those cases surface variance supersedes any possible atmospheric effects.

region was previously studied by *Greeley and Guest* [1987], based on Viking data. Those authors differentiated between northern Noachian and southern Hesperian units. Their Noachian "Etched unit" was interpreted as a cratered unit partly mantled by possibly aeolian deposits, and dissected by aeolian, ground ice and fluvial activity; according to the same authors, a number of NE trending fractures and graben filled with younger aeolian materials cut across this unit. Their Hesperian "Syrtis Major formation" was interpreted as corresponding to low-viscosity lava flows, rheologically similar to basaltic magmas, with radial mare-type wrinkle ridges. The highland-lowland dichotomy boundary runs from the NW to the SE across the northern terrains in this region. Later studies based on the analysis of TES spectroscopic data [*Hoefen et al.*, 2000, 2003; *Hoefen and Clark*, 2001; *Hamilton et al.*, 2001, 2003] unveiled a 30,000-square-kilometer area rich in olivine, the largest deposit of this mineral known to date on Mars.

[36] The thermal inertia (Figure 13a) and albedo (Figure 13b) properties of the surface materials in this region, summarized in Table 4, indicate duricrust deposits and rocky regions are dominant in the area (Figures 13c and 13d). In our analysis of the TES spectral data, seven data-derived end-members were identified (Figure 13e), inter-

Figure 11. Spectral and thermophysical properties of the Amazonis Planitia study area: (a) TES-derived thermal inertia map. (b) TES-derived albedo map. (c) Two-dimensional histogram of albedo versus thermal inertia values showing correspondence to the global thermophysical units defined by *Mellon et al.* [2000] and *Putzig et al.* [2005]: yellow, global units A and C; green, global unit C; red, global unit B. (d) Spatial distribution of the thermophysical units superimposed to MOC visible data. Same color scheme as Figure 11c. (e) TES-derived spectral end-members: yellow, dust; red, surface type 1 (basaltic materials); blue, atmospheric water ice; green, instrument noise. (f) Spatial distribution of the closest matches to the TES-derived end-members superimposed to MOC visible data. Same color scheme as in Figure 11e.

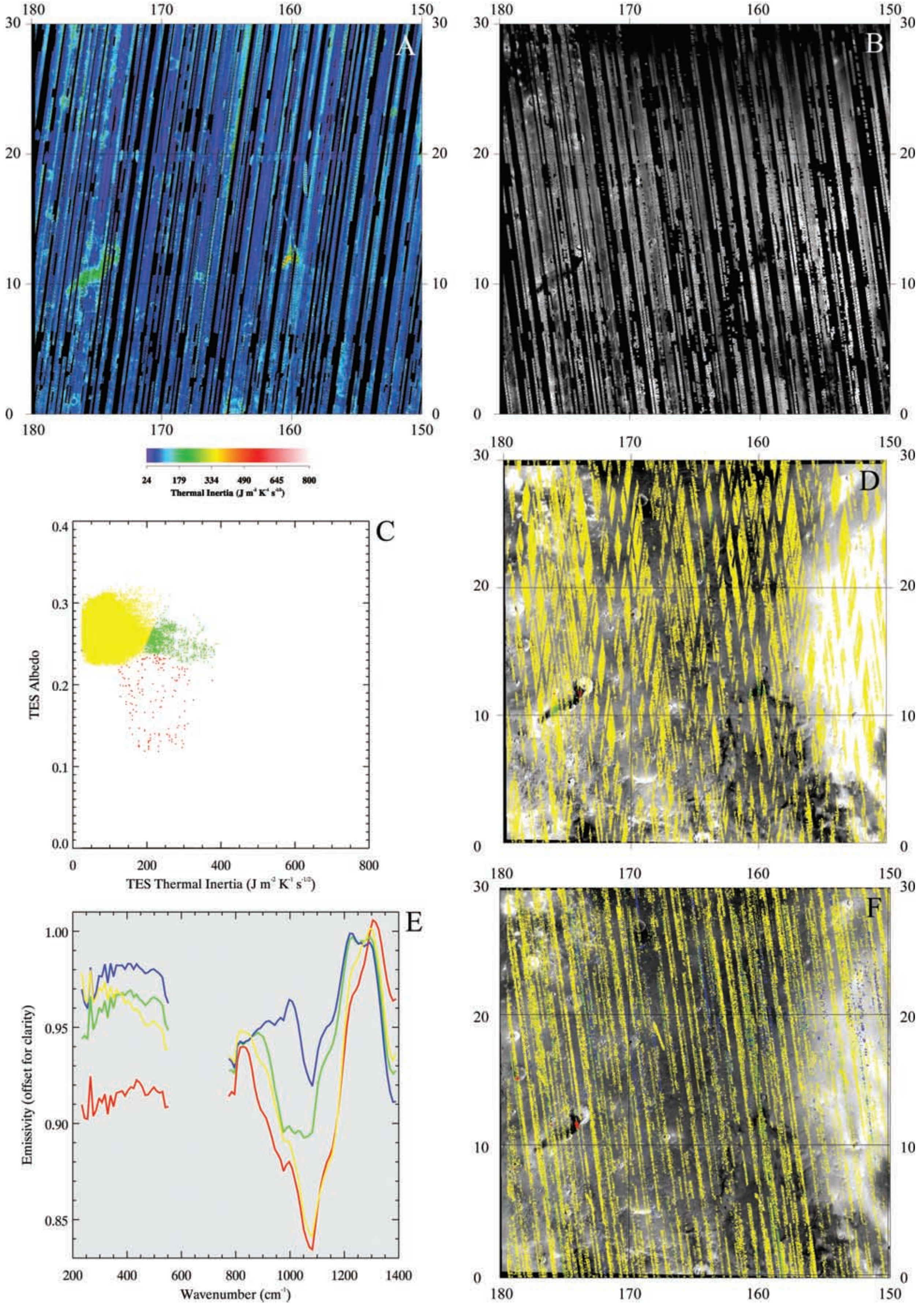
A
B
C
D
E
F
180
170
160
150
30
20
10
0
24
179
334
490
645
800
Thermal Inertia (J m⁻² K⁻¹ s⁻¹ᐟ²)
TES Albedo
0.4
0.3
0.2
0.1
0.0
0
200
400
600
800
TES Thermal Inertia (J m⁻² K⁻¹ s⁻¹ᐟ²)
Emissivity (offset for clarity)
1.00
0.95
0.90
0.85
200
400
600
800
1000
1200
1400
Wavenumber (cm⁻¹)

Figure 11

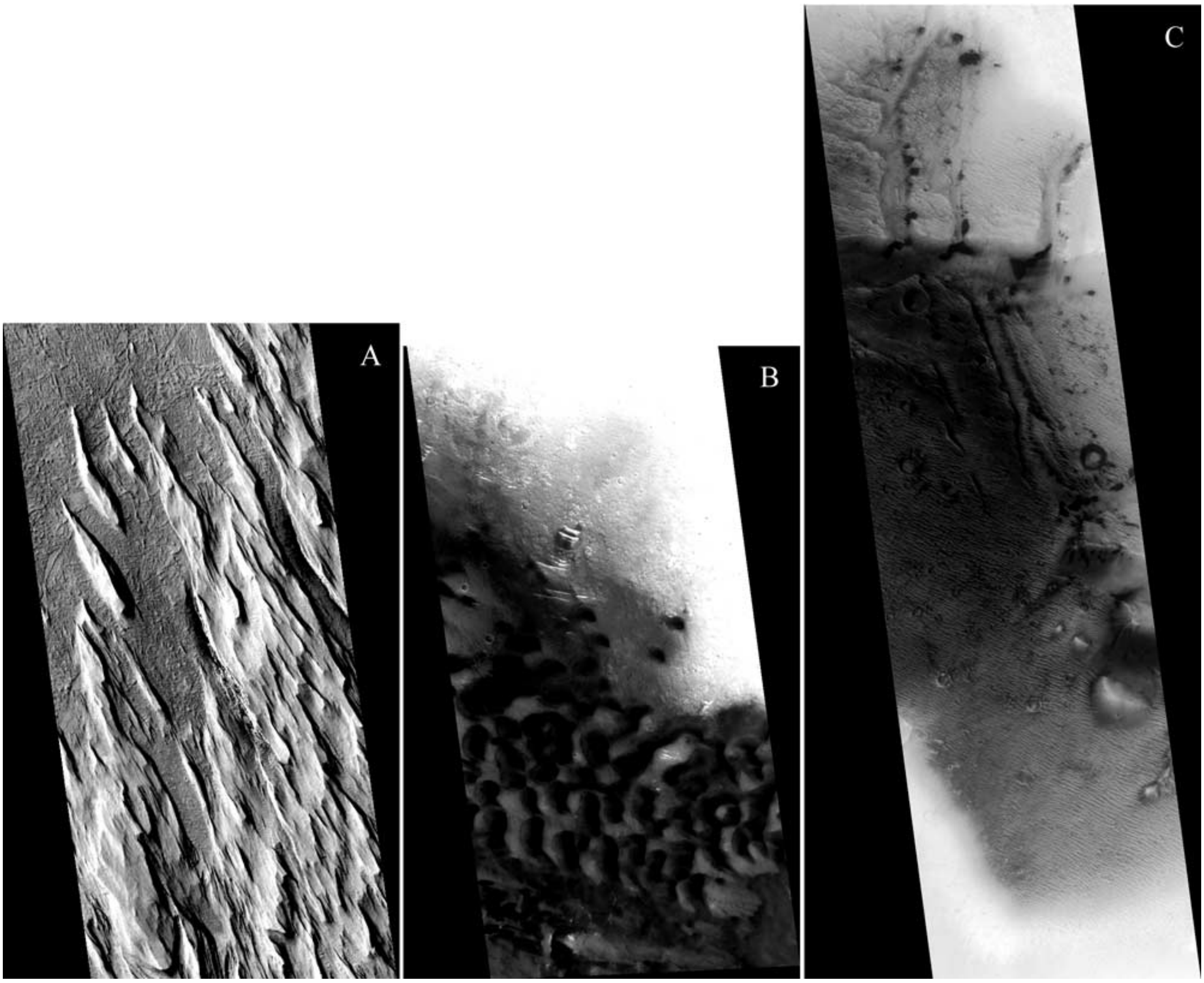

Figure 12. Morphological features at Amazonis Planitia as seen in MOC narrow angle images. (a) Detail of scene E0100801 centered at 12.94°N, 159.84°W, showing yardangs corresponding to a duricrust area. Their TES spectral signature is consistent with that of dust. (b) Detail of scene M0303621, centered at 11.87°N, 174.08°W, showing low albedo dunes inside Pettit Crater. Their TES spectra is indicative of basaltic materials. (c) Detail of scene M2100488 centered approximately at 15.32°N, 178.64°W, inside an unnamed crater: low albedo dunes coincide spatially with TES basaltic signature. The low albedo materials are circumscribed by rectilinear, graben-like depressions that suggest subsurface collapse.

preted as airborne water-ice aerosols, instrument noise like that described by *Bandfield* [2002], surface dust, surface type 1 materials, surface type 2 materials (interpreted as andesitic [*Bandfield et al.*, 2000] or altered basaltic materials [*Wyatt and McSween*, 2002]), olivine, and phyllosilicates and/or high-Si glass. Figure 13f illustrates the spatial distribution of these end-members; instrument noise and atmospheric water-ice have not been mapped for clarity. It is worthwhile noticing, though, that the end-member interpreted as atmospheric water-ice is almost exclusively

Figure 13. Spectral and thermophysical properties of the Nili Fossae study area: (a) TES-derived thermal inertia map. (b) TES-derived albedo map. (c) Two-dimensional histogram of albedo versus thermal inertia showing correspondence to the global thermophysical units defined by *Mellon et al.* [2000] and *Putzig et al.* [2005]: green, global unit C; red, global unit B; blue, global unit F. (d) Spatial distribution of the thermophysical units superimposed to MOC visible data. Same color scheme as Figure 13c. (e) TES-derived spectral end-members: yellow, dust; blue, atmospheric water ice; green, olivine; red, surface type 1; purple, surface type 2; dark green, instrument noise; pink, phyllosilicates/high-Si glass. (f) Spatial distribution of the closest matches to relevant TES-derived end-members superimposed to MOC visible data (atmospheric water-ice and instrument noise not mapped for clarity). Same color scheme as in Figure 13e; white circles indicate location of spectra consistent with phyllosilicates/high-Si glass.

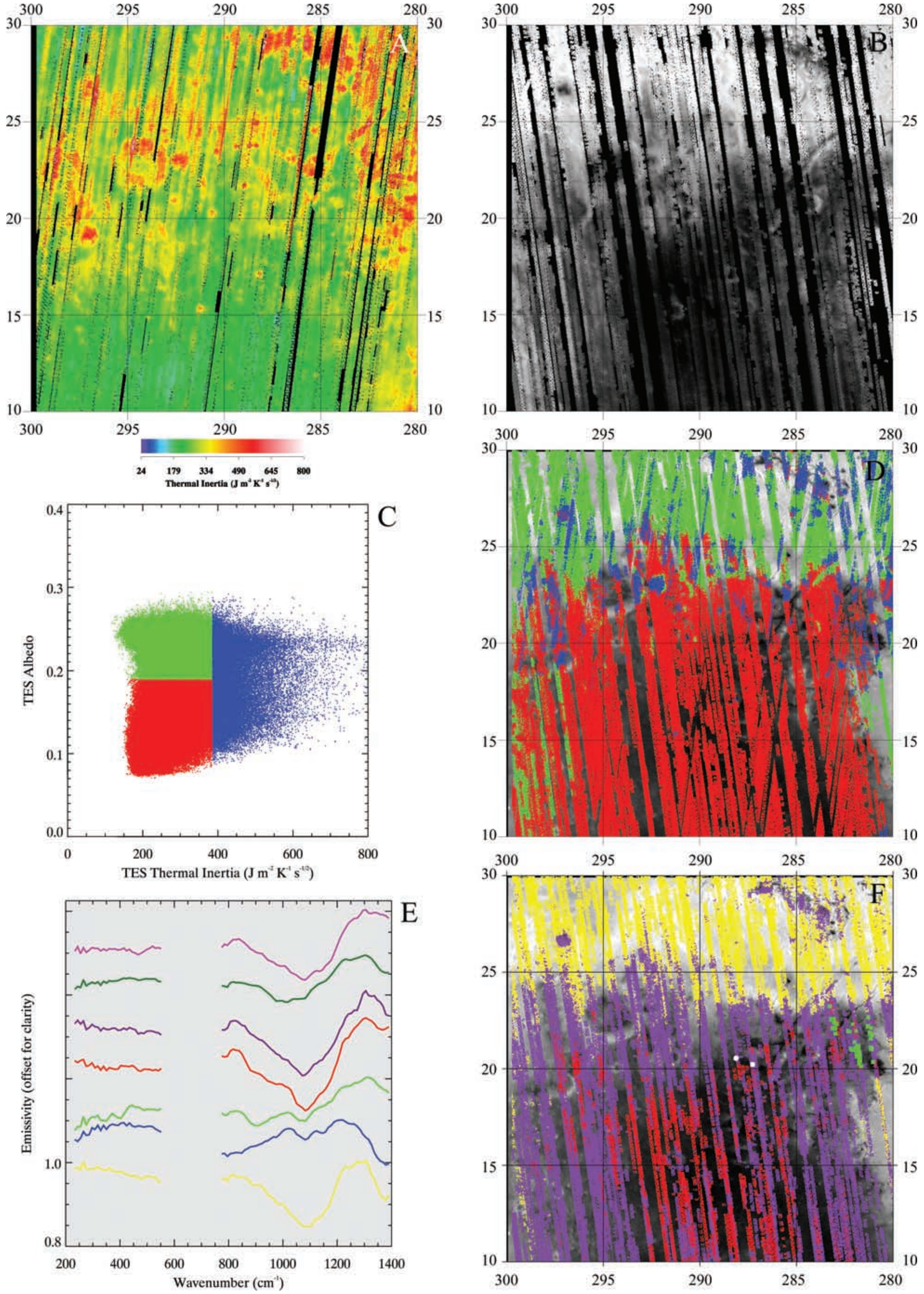
A
B
C
D
E
F
300
295
290
285
280
30
25
20
15
10
24
179
334
490
645
800
Thermal Inertia (J m^{-2} K^{-1} s$^{-1/2}$)
TES Albedo
0.0
0.1
0.2
0.3
0.4
TES Thermal Inertia (J m^{-2} K^{-1} s$^{-1/2}$)
0
200
400
600
800
Emissivity (offset for clarity)
0.8
1.0
Wavenumber (cm^{-1})
200
400
600
800
1000
1200
1400

Figure 13

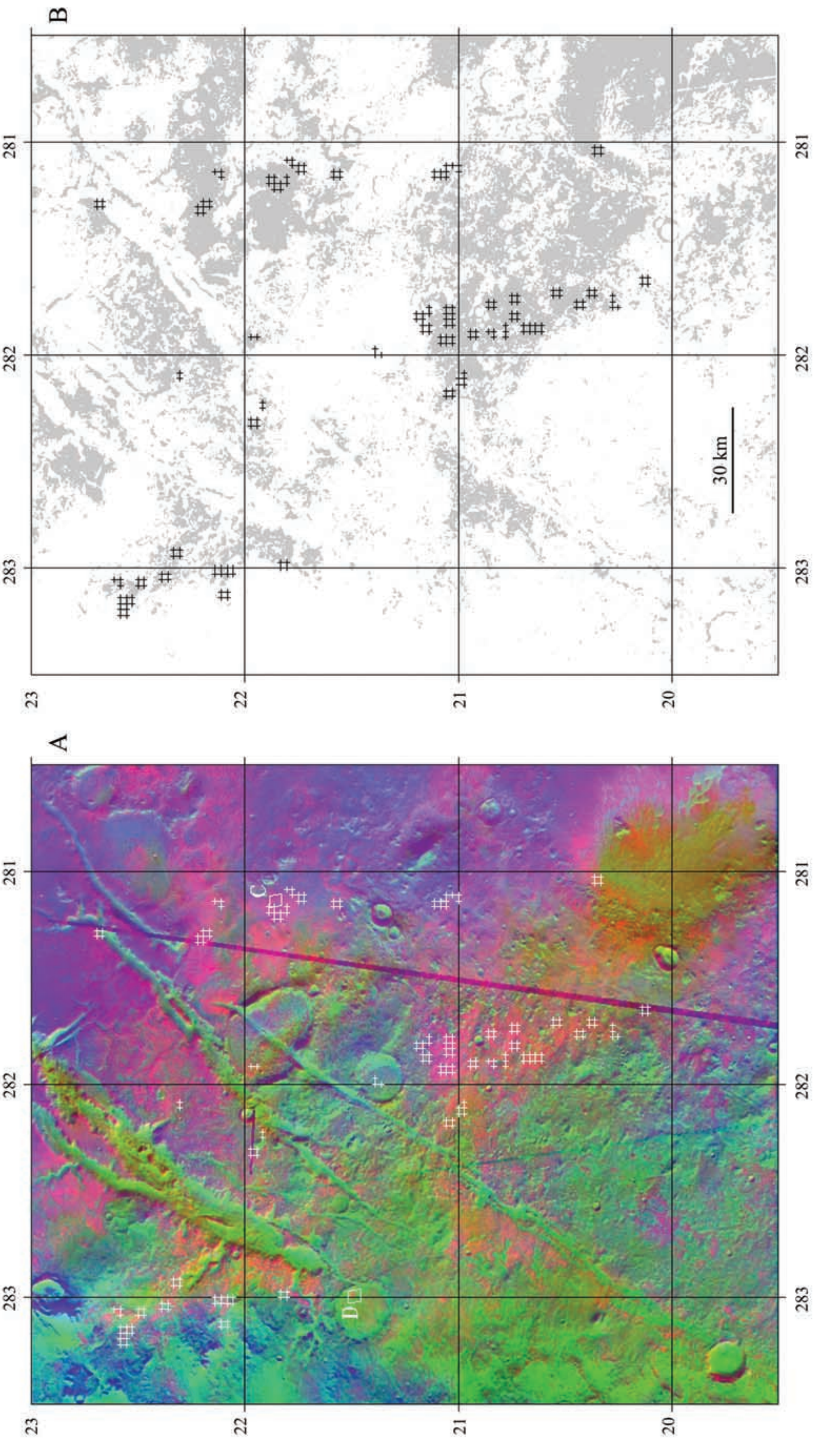

Figure 14

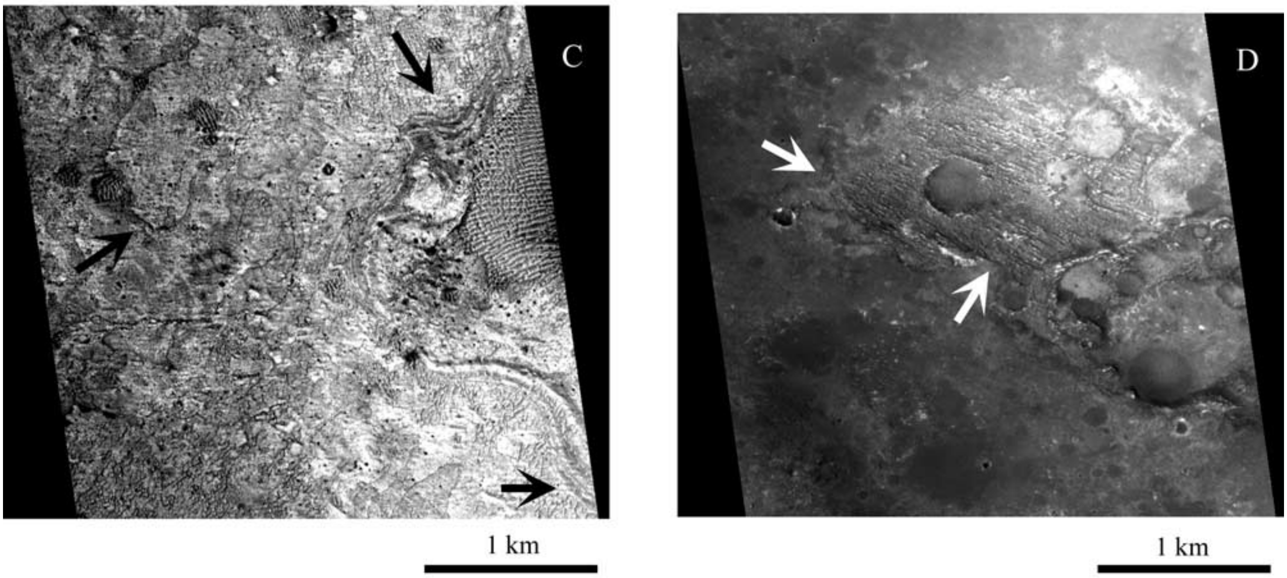

Figure 14. (continued)

present in the northern part of the study area, where the dominant surface spectral end-member is consistent with dust. Dust-dominated surfaces coincide with the thermophysical unit interpreted as duricrust; olivine, surfaces type 1 and 2, and phyllosilicates/high-Si glass are present in the rocky regions.

[37] On the basis of the spectral libraries available the olivine data-derived end-member is forsteritic in composition; this interpretation is in agreement with previous studies [*Hoefen and Clark*, 2001; *Hoefen et al.*, 2003]. The olivine appears concentrated in a region to the E of the study area; for analysis of surface morphologies in that region, spatial context, and depiction of detailed diurnal temperature variations, we derived nighttime and daytime brightness temperature mosaics from high spatial resolution THEMIS IR band 9 data as described by *Martínez-Alonso et al.* [2005], and then combined them in a false color composite (Figure 14a) with a MOC red-band wide-angle mosaic (produced by Malin et al., available at http://www.msss.com/mgcwg/mgm). The olivine occurs within a distinct unit (Figure 14b), which exhibits less pronounced diurnal temperature variations than its surroundings, indicative of relatively higher thermal inertia values, and consistent with the TES-derived thermal inertia values observed (600–790), among the highest in the region. The surface morphology of the olivine-rich unit is rough at THEMIS IR scale due to impact cratering and erosion, shows horizontal layering, and has low albedo values, close to 0.1 in average (Figure 14c). Contrasting with this unit, surrounding materials have darker albedo (average 0.08), pristine surfaces almost unaffected by cratering and denoting its young age, quasi-circular features suggestive of buried craters, and lobate boundaries (Figure 14d); materials of similar characteristics fill the fossae in the region. The olivine deposit at Nili Fossae was tentatively dated as Hesperian by *Hoefen et al.* [2003], who interpreted it as consistent with exposure by Isidis impact-related faulting of an older, underlying olivine-rich layer. We found undisturbed olivine-rich unit exposures in, among other places, the interior of a large impact crater centered at 21.89°N, 281.78°W, indicating the unit is not part of an older basement. We interpret the olivine-rich unit as post-Isidis-impact volcanic or volcano-sedimentary materials, subsequently eroded and finally overlaid by younger volcanic flows probably extruded through the fossae in the region.

[38] A small number of TES spectra in the study area were identified as consistent with a high-Si glass (J. Bandfield,

Figure 14. (a) False color image showing thermophysical units in the olivine-rich area of Nili Fossae; brighter colors indicate higher values in the corresponding band. Red band: THEMIS nighttime temperature mosaic. Green band: THEMIS daytime temperature mosaic. Blue band: MOC red wide-angle mosaic. TES spectra identified as olivine in this study are shown with white crosses; because of incomplete TES coverage (see Figure 13f for reference), this is most probably an underestimate of the actual olivine present in the region. Reddish tones correspond to the olivine-rich unit, greenish tones to a darker, smoother unit; bluish tones to high albedo surfaces. White boxes indicate location of Figures 14c and 14d. (b) Approximate outline of the olivine-rich unit, which may also occur in the northern and eastern portions of this area, under high albedo deposits (see purple areas in Figure 14b); further spectroscopic analysis are required to map the actual olivine occurrences throughout this unit. (c) Subset of MOC narrow-angle scene E0500108, centered at 281.14°W, 21.86°N; arrows indicate layering in the olivine-rich unit. (d) Subset of MOC narrow-angle scene R0100614, centered at 282.99°W, 21.49°N; arrows show the contact between the olivine-rich unit (brighter albedo, rough surface morphology) and younger surrounding materials (darker albedo, smooth surfaces, lobate boundaries).

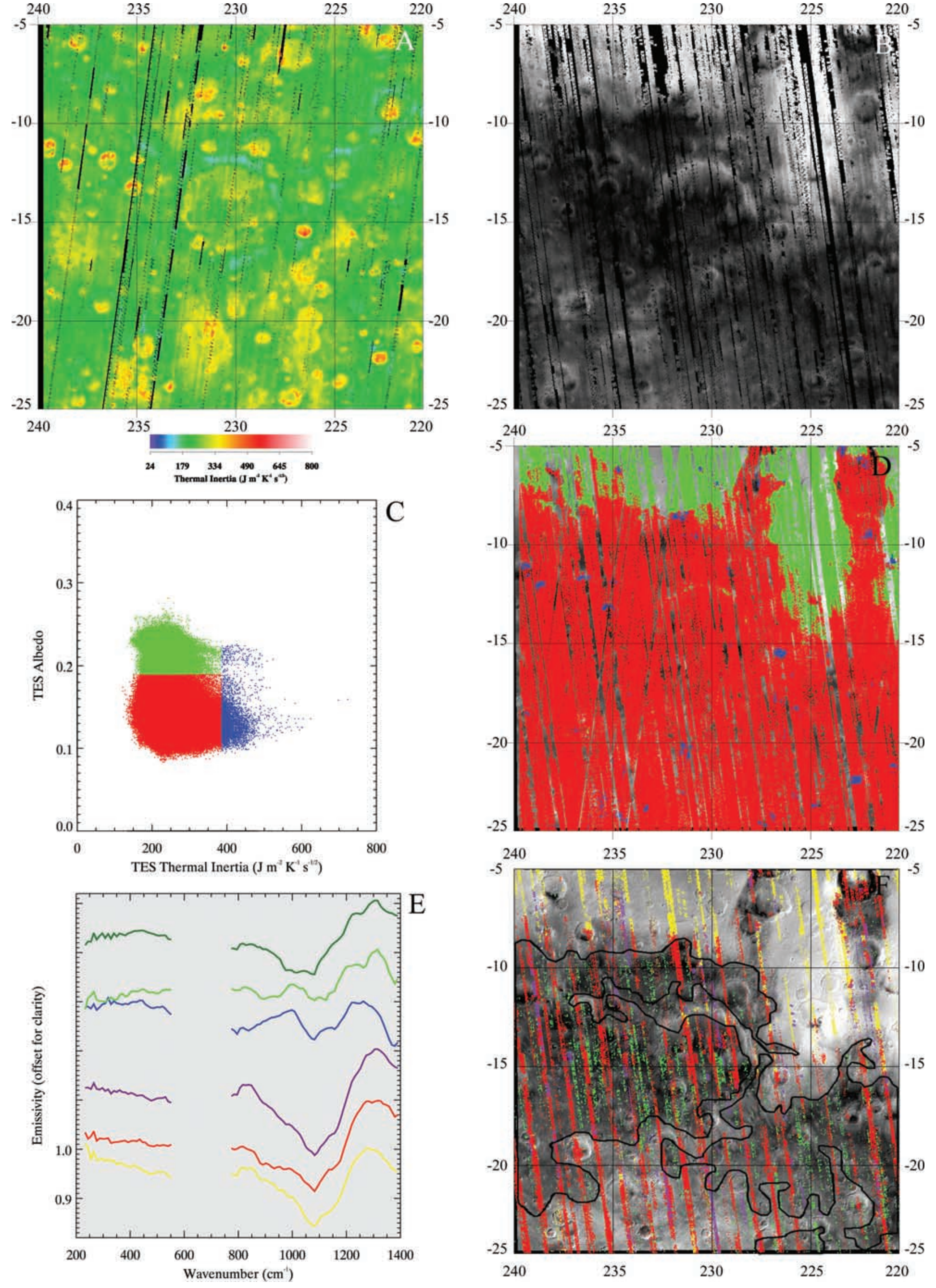
A
B
C
D
E
F
240
235
230
225
220
-5
-10
-15
-20
-25
24
179
334
490
645
800
Thermal Inertia (J m-2 K-1 s-1/2)
TES Albedo
0.0
0.1
0.2
0.3
0.4
TES Thermal Inertia (J m-2 K-1 s-1/2)
0
200
400
600
800
Emissivity (offset for clarity)
1.0
0.9
Wavenumber (cm-1)
200
400
600
800
1000
1200
1400

Figure 15

personal communication, 2002) and/or phyllosilicate end-member, not reported in the region prior to this investigation. This end-member's identification was corroborated by deconvolution with atmospheric removal of selected TES spectra (J. Bandfield, personal communication, 2004), which yielded the following results: 33% plagioclase, 32% phyllosilicates/high-Si glass, and other components below the method's detection limit, such as pyroxene, olivine, sulfates, and carbonates. We find this end-member mainly clustered in two locations: near 29.08°N, 287.31°W, spatially associated with surface type 2 materials; and near 20.25°N, 287.70°W, close to the boundary between surface type 1 and 2 materials. The THEMIS and MOC imagery inspected failed to show morphological, albedo, or surface temperature-related characteristics unique to the occurrences of this spectral end-member in the TES data. A spectral signature consistent with a volcanic glass, phyllosilicate, or zeolite component was also identified in TES spectral data at Nili Patera (800 km south of the Nili Fossae study area) by *Ruff and Christensen* [2003]; this may indicate that, although not a major surface component, this end-member may be present over large areas in the region.

3.4. Analysis of the Mare Tyrrhenum Region

[39] The Mare Tyrrhenum study area presents higher than average SVI values (Table 2). *King* [1978] found this region to be mostly occupied by ancient impact breccias; melts and volcanic rocks ejected from basins such as the Hellas Basin; older and younger crater ejecta, mantled by aeolian deposits preferentially located inside craters, and interleaved with some volcanic rocks; and basaltic lava flows overlaying the northern section. The same authors found evidence they interpreted as erosional features indicative of aqueous erosion and deposition. Subsequently, *Greeley and Guest* [1987] assigned Noachian age to most of the materials in the region (volcanic and erosional materials, mixed with impact breccias), except for the intracrater deposits they dated as Hesperian. They also mapped thin lava flows and sedimentary deposits in the western part of the study area; ridged plains materials found inside and surrounding some craters throughout the region were also interpreted by *Greeley and Guest* [1987] as low-viscosity lava flows.

[40] The thermal inertia and albedo properties of this study area (Figures 15a and 15b), summarized in Table 5, are mostly consistent with those of rocky surfaces and indurated materials. Thermophysical units were separated and identified based on the thresholds proposed by *Putzig et al.* [2005] (Figure 15c), and then mapped back into the spatial domain (Figure 15d). Although distinct, the spatial boundary between the northern terrains dominated by duricrust and the southern, predominantly rocky regions, does not correspond to a clear morphological feature.

[41] Analysis of the TES spectral data indicates the presence of the following data-derived end-members: airborne water-ice aerosols, instrument noise similar to that described by *Bandfield* [2002], surface dust, surface type 1 materials, an "undetermined" end-member discussed below, and, tentatively, surface type 2 materials (Figure 15e). Figure 15f illustrates the spatial distribution of surface-related, data-derived spectral end-members; instrument noise and atmospheric water-ice have not been mapped for clarity. The spatial distribution of the "undetermined" end-member was refined utilizing a spectral index based on the depth of its most characteristic absorption band, centered near 891 cm^{-1} ($\varepsilon 2$), respect to the emissivity maxima near 785 ($\varepsilon 1$) and 997 cm^{-1} ($\varepsilon 3$): $[(\varepsilon 1 + \varepsilon 3)/\varepsilon 2]$; index values above 2.03 were found to correspond to a distinct set of spectra further described below. Dust spectral signatures coincide mostly with the duricrust-dominated surfaces in the northern third of the study region. As in the Nili Fossae region, the end-member interpreted as atmospheric water-ice is almost exclusively present where the dominant surface spectral end-member is dust.

[42] The rocky regions can be subdivided into two domains: one corresponds to topographically elevated regions of rough morphology, the other to topographically lower regions, generally smoother and with wrinkle-ridge-like features. The two domains have slightly different albedo (averaging approximately 0.13 in the higher terrains versus 0.12 in the lower) and thermal inertia (240 and 320, respectively; approximate averaged values corresponding to intercrater zones). The "undetermined" spectral end-member is mostly constrained to the lower, darker regions of higher thermal inertia, while surface type 1 materials are found in both domains. This end-member cannot be explained by spectral mixing of the other data-derived end-members in the region; its spatial distribution is consistent with other surface properties, indicating that it corresponds to a distinct surface unit rather than to instrument noise or atmospheric effects. The "undetermined" end-member presents distinct absorption bands approximately centered at 891 and 944 cm^{-1}, as well as a shallower band near 477 cm^{-1}; an emissivity maximum near 400 cm^{-1} separates the latter from less clear bands which occur occasionally in the 300–380 cm^{-1} range (Figure 16). According to the spectral libraries available we find the most plausible assignment for this end-member to be volcanic materials (as inferred from thermophysical and morphological evidence) with elevated amounts of olivine of fayalitic composition; volcanic materials with elevated amounts of high-Ca clinopyroxenes

Figure 15. Spectral and thermophysical properties of the Mare Tyrrhenum study area: (a) TES-derived thermal inertia map. (b) TES-derived albedo map. (c) Two-dimensional histogram of albedo versus thermal inertia values showing correspondence to the global thermophysical units defined by *Mellon et al.* [2000] and *Putzig et al.* [2005]: green, global unit C; red, global unit B; blue, global unit F. (d) Spatial distribution of the thermophysical units superimposed to MOC visible data. Same color scheme as Figure 15c. (e) TES-derived spectral end-members: yellow, dust; red, surface type 1; purple, surface type 2; blue, atmospheric water ice; green, "undetermined"; dark green, instrument noise. (f) Spatial distribution of the closest matches to the TES-derived surface end-members superimposed to MOC visible data (atmospheric water-ice and instrument noise not mapped for clarity). Same color scheme as in Figure 15e. Black lines highlight low-albedo, low-elevation terrains where most of the "undetermined" end-member occurs; see text for discussion.

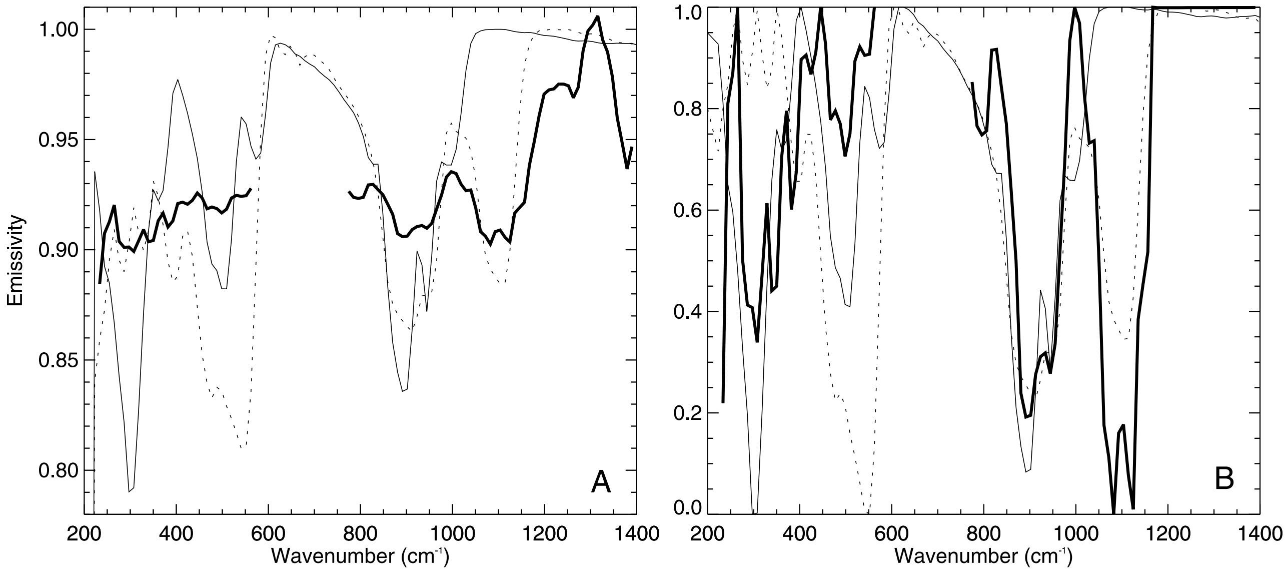

Figure 16. (a) Comparison between a TES spectrum representative of an "undetermined" data-derived end-member extracted from the Mare Tyrrhenum data set (thick line) and library spectra [*Christensen et al.*, 2000c] of fayalite (thin line) and augite (dotted line). Library spectra were convolved to TES resolution; no contrast enhancement or scaling was applied to any these spectra. (b) The same spectra normalized. There is good correspondence between fayalite and the TES spectra regarding both the location and relative depth of the characteristic bands centered near 300, 477, 891, and 944 cm^{-1}. The band near 1100 cm^{-1} is ubiquitous in TES data and corresponds to dust.

(e.g., augite, diopside, and hedenbergite, among others) offer a second-best fit. The spectra of both olivines and pyroxenes are dominated by SiO_4 stretch and bend fundamentals; they are roughly analogous, as expected from their compositional and structural similarities. However, the available library spectra of clinopyroxenes coincide in presenting their deepest emissivity bands near 500–540 cm^{-1}, and shallower bands near 300 and 900 cm^{-1} (Figure 16b); the opposite is true for the "undetermined" spectra, as well as for fayalite library spectra. Fayalite has a deep band near 300 cm^{-1} which is not always clearly present in the "undetermined" spectra; lower instrument signal-to-noise ratio at low wave numbers [*Christensen et al.*, 2000b], emission by atmospheric water vapor, and/or grain size effects [*Salisbury et al.*, 1991], may be some of the causes of this disagreement.

[43] The surface type 2 signature is sparse in the region; its distribution coincides in many cases with orbital ground tracks which may be indicative of interfering atmospheric effects (e.g., dustier atmosphere); according to this, an alternative interpretation for this end-member could be surface type 1 materials as seen under dustier atmospheric conditions.

4. Discussion

4.1. Comparison Between the SVI Maps and Other Global Surface Properties

[44] The spatial distribution of SVI values is remarkably coherent: high and low SVI value cells appear clustered in separate, discrete geographic areas; it is also similar to other global surface properties, such as albedo, thermal inertia, and global mineral distribution.

[45] Thermal inertia, albedo, and SVI measure intrinsically different properties of the surface: grain size/compaction, brightness, and composition-related diversity, respectively. However, they show some broad similarities in their spatial distribution. Areas of low SVI value (≤ 2, Figure 17a) coincide spatially with areas of high albedo (≥ 0.2, Figure 17b) and low thermal inertia (≤ 150, Figure 17c) such as Arabia Terra, Elysium Planitia, Amazonis Planitia, Tempe Terra, Xante Terra, Hellas Planitia, Promethei Terra, Argyre Planitia, and Noachis Terra. High-albedo, low-thermal inertia regions are commonly interpreted as covered by mostly uniform dust and/or duricrust. Consequently, they would be consistent with spectrally homogeneous regions at TES resolution. Conversely, high SVI values (≥ 3) occur in low-albedo (≤ 0.2), high-thermal inertia (≥ 150) regions such as Syrtis Major Planum, Nili Fossae, Terra Tyrrhena, Valles Marineris, Margaritifer Terra, Acidalia Planitia, and Terra Meridiani. Low-albedo and high thermal inertia values are considered indicative of exposed rocky surfaces, potentially more diverse than dust- or duricrust-covered regions, and consequently leading to larger spectral diversity. The similarities between the spatial distribution of SVI and those of thermal inertia and albedo are not one-to-one, indicating that those parameters are complementary.

[46] Some of the high SVI regions identified in this analysis coincide with regions of previously known mineralogical interest, such as Nili Fossae [*Hoefen et al.*, 2000, 2003; *Hoefen and Clark*, 2001; *Hamilton et al.*, 2001, 2003] and Ganges Chasma, in Valles Marineris [*Christensen et al.*, 2003], where olivine deposits have been identified; and Sinus Meridiani [*Christensen et al.*, 2000a, 2001a], the site of a large deposit of crystalline hematite. To compare the

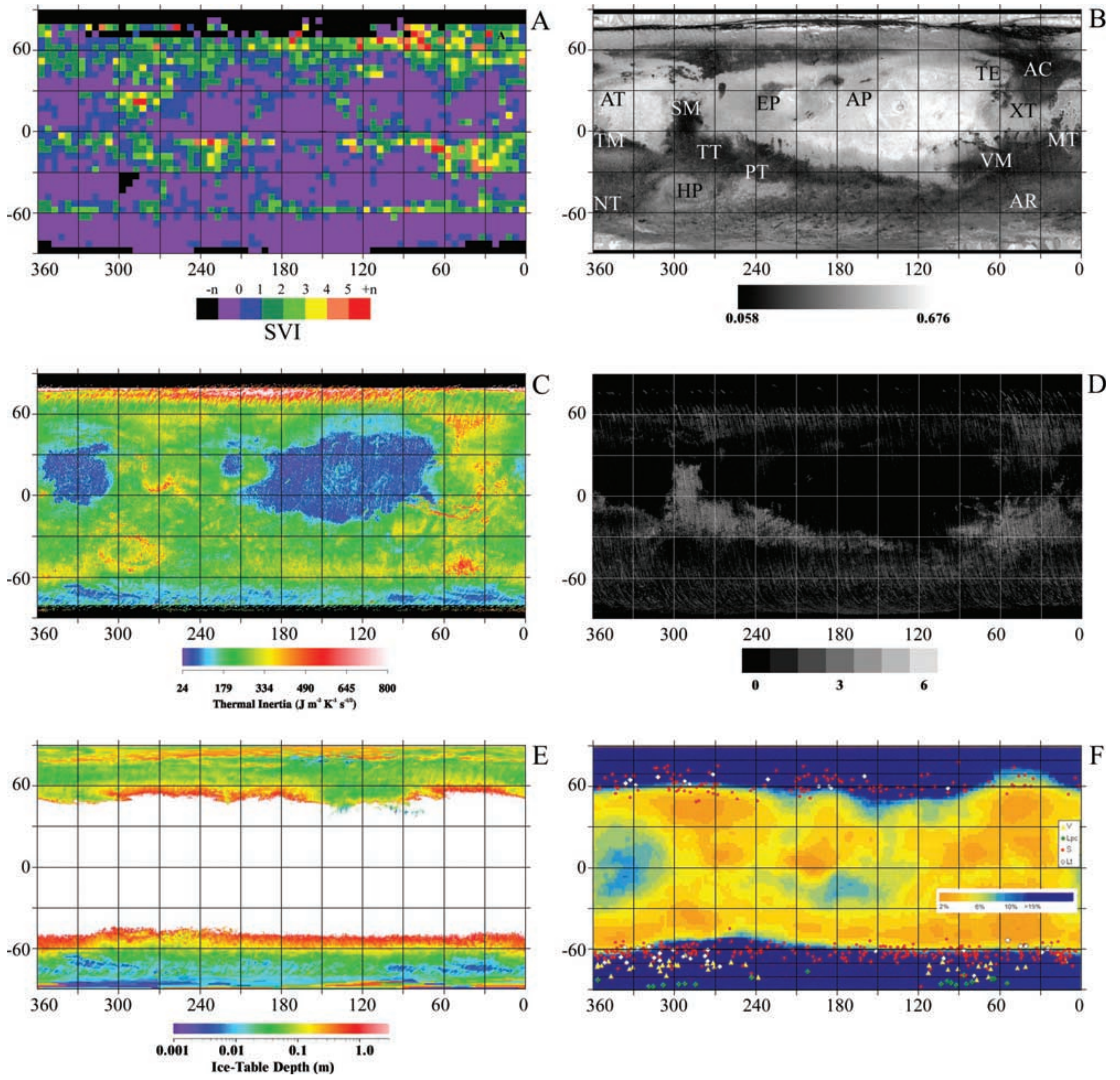

Figure 17. Comparison between SVI and other global surface properties. (a) SVI map derived from spectral range 1 + 2. (b) Albedo [data from *Pelkey and Jakosky*, 2002]. Labels identify regions discussed in the text: AT, Arabia Terra; TM,Terra Meridiani; NT, Noachis Terra; SM, Syrtis Major; TT, Terra Tyrrhena; HP, Hellas Planitia; EP, Elysium Planitia; PT, Promethei Terra; AP, Amazonis Planitia; TE, Tempe Terra; XT, Xante Terra; VM, Valles Marineris; AR, Argyre Planitia; AC, Acidalia Planitia; MT, Margaritifer Terra. (c) Thermal inertia [data from *Mellon et al.*, 2000]. (d) Surface mineralogy index derived from data from *Bandfield* [2002] (see text for details). (e) Ice-table depth, white indicates regions of ground-ice instability [modified from *Mellon et al.*, 2004]. (f) Distribution of small (<40 m) homogeneous polygons (red circles) overlaid to ground ice proportion map [modified from *Mangold et al.*, 2004].

SVI results to preexisting global mineral distribution maps [*Bandfield*, 2002], an independent estimate of surface mineralogy variability was derived from the latter. The global mineral maps were derived from deconvolution of TES spectral data [*Bandfield et al.*, 2000], and represent the spatial distribution at 0.25 × 0.25 degree resolution of the following mineral groups: quartz, K-feldspar, plagioclase, amphibole, low-Ca pyroxene, high-Ca pyroxene, olivine, hematite, sulfates, carbonates, and combined phyllosilicates and high-Si glass. We converted each of the eleven mineral maps into binary maps showing either presence above the detection limit (0.1) or absence for each mineral class; the binary maps were then added up. The resulting surface mineralogy variability index map is shown in Figure 17d;

values range between 0 (no minerals were mapped above the detection limit) and 6 (the deconvolution technique identified up to six types of minerals above the detection limit). This map mimics closely the spatial distribution of surface albedo; its highest values are found coinciding with high SVI values in low albedo regions such as Syrtis Major, Terra Meridiani, Margaritifer Terra, Terra Tyrrhena, Valles Marineris, and Acidalia Planitia. Conversely, the lowest values in the index map coincide with low SVI values.

[47] The SVI maps show latitudinal bands of relatively high values near 60°N and 60°S: the southern band appears circumscribed to a narrow latitudinal range and is better delineated, the northern band is wider and more irregularly shaped. Extremely high SVI values above latitude 60°N are not considered significant, because of the very low number of spectra per cell in those regions; they may be mostly caused by instrument noise induced by low temperatures and/or extreme atmospheric conditions. However, both the regional trend toward increasing SVI values above 45°N and the high-SVI band near 60°S are considered consistent with actual surface properties. Those high SVI latitudinal bands coincide spatially with bands of low albedo and high thermal inertia (Figures 17b and 17c); their thermophysical properties coincide with those of surfaces dominated by rocks and bedrock [*Mellon et al.*, 2000; *Putzig et al.*, 2005]. Deconvolution results [*Bandfield*, 2002] indicate that those high-latitude bands are mineralogically more diverse than most of the rest of the planet (Figure 17d). Those bands are in close proximity to the subsurface ice stability boundary [*Mellon et al.*, 2004] (Figure 17e) and to regions characterized by the presence of small (<40 m), homogeneous polygons [*Mangold et al.*, 2004] (Figure 17f), similar to terrestrial ice-wedge polygons. The high SVI bands also coincide with the poleward limits of dissected mantled terrains [*Mustard et al.*, 2001; *Head et al.*, 2003], interpreted as disaggregating deposits cemented by ice. These observations suggest that the high SVI latitudinal bands may be the compositional surface expression of climate-related processes previously recognized through morphological features; such processes may be churning the regolith, exposing rockier and/or coarser-grained surfaces relative to a dust coating.

4.2. Comparison Between SVI Values and Ground Truth Data

[48] Data acquired in situ by the five Martian landers (Viking Landers 1 and 2, Pathfinder, and Mars Exploration Rovers Spirit and Opportunity) corroborate the SVI results. Viking Lander 1 (Chryse Planitia) touched down in a plain exhibiting bedrock, rocks, indurated materials, and dust [*Arvidson et al.*, 1989]. Fine-grained, palagonite-like materials, as well as dark rocks similar to mafic igneous rocks were identified in the landing area by analysis of visible and near-infrared multispectral imagery. Viking Lander 2 (Utopia Planitia) landed at the edge of the deposits ejected from Mie, a large impact crater. Rock fragments, duricrust, and aeolian drifts constitute the surface deposits observed in the region; the rocks were found to be consistent with dark, iron-rich igneous rocks, the fine-grained deposits with palagonitic materials [*Arvidson et al.*, 1989]. The Pathfinder's landing site (Ares Vallis in Chryse Planitia) presented a rocky surface with aeolian deposits and some indurated materials [*Golombek et al.*, 1997]. X-ray spectrometer data obtained from the rocks at this site indicate they are basaltic to andesitic in composition [*Rieder et al.*, 1997; *Wänke et al.*, 2001]; some had textures indicative of a volcanic origin [*Golombek et al.*, 1997]. The soils and dust at this landing site were consistent with poorly crystalline or nanophase ferric oxides [*Bell et al.*, 2000] with Mg-sulfate and -chloride [*Wänke et al.*, 2001). The Rover Spirit (Gusev Crater) encountered a similar landscape, consisting of rock fragments, fine-grained deposits, and duricrust. The rocks analyzed to date were interpreted as olivine-bearing basalts [*Squyres et al.*, 2004b; *McSween et al.*, 2004; *Christensen et al.*, 2004c]. To sum up, Viking Landers 1 and 2, Pathfinder, and Spirit landed in similar regions dominated by fragments of dark igneous rocks, fine-grained materials, and some duricrust. This is consistent with the very low SVI values of the 5 × 5 degree cells containing those landing regions (−1.2, 0.5, −0.4, and −0.3, respectively). According to these values, those four landers coincided in probing localities representative of the most spectrally bland, even below the average, regions exposed in the surface of that planet (Table 2).

[49] By contrast, The Mars Exploration Rover Opportunity (Sinus Meridiani) landed on a region of relatively more complex mineralogy/lithology: hematite, olivine, jarosite, and other sulfates have been identified to date by Opportunity as constituents of the fine materials and some of the rocks in the landing area. Rock fragments of basaltic composition as well as rock outcrops putatively identified as sedimentary [*Squyres et al.*, 2004c] or volcano-sedimentary in origin were also identified. The surface materials diversity encountered by Opportunity is consistent with the elevated SVI value of the 5 × 5 degree cell containing the landing area (2.7), significantly above the average of the planet (Table 2).

[50] The areas sampled by the landers are very small (in the order of meters to a few kilometers), compared to those sampled in the SVI derivation (5 × 5 degree cells, equivalent to 300 × 300 km regions in the equatorial regions). Despite the obvious differences in sampling scale, the degree of spectral diversity determined with the SVI method is remarkably consistent with that observed in the landers' data.

4.3. Significance of Some of the Spectral End-Members Identified and Comparison to Spectral Deconvolution Results

[51] The spectral end-members identified in the three study areas are indicative of a geological history dominated by volcanism (surface type 1 and 2 materials), lack of prevalent chemical weathering in extensive regions (olivine), and surficial/atmospheric processes resulting in the induration of fine materials (dust). Further analysis are required to elucidate the nature and hence significance of the end-member identified as phyllosilicate and/or high-Si glass. Atmospheric water-ice and instrument noise end-members were also identified.

[52] The surface dust end-member identified in all three regions coincides spatially with surfaces of thermophysical properties characteristic of bright, unconsolidated fine materials (dust deposits), or duricrust-dominated surfaces. In Nili

Fossae and Mare Tyrrhenum we observed that the spectral end-member interpreted as atmospheric water-ice is relegated to regions of thermophysical properties consistent with duricrust and spectrally dominated by the signature of dust. Extending this assessment to the Amazonis Planitia study area is not possible due to the lack of substantial areas occupied by materials of spectral characteristics different from those of dust. The relatively high surface temperatures through the study areas ($\geq$250 K) would not allow for the available atmospheric water vapor to saturate [*Mellon and Jakosky*, 1995] and form surface frosts during the daytime; the water-ice end-member detected is therefore consistent with atmospheric rather than surface condensation. The spatial coincidence with a surface unit suggests the atmospheric water-ice is not brought from elsewhere. Topography does not justify elevated amounts of water vapor (and hence water-ice) in those areas spectrally dominated by dust. Further analyses are required to investigate seasonal effects on the water-ice distribution; its high frequency of occurrence suggests seasonality is not a main governing factor. We suggest possible mechanisms to explain the observed distribution of atmospheric water-ice in regions dominated by surface dust/duricrust: (1) daytime sublimation of nighttime frosts, (2) desorption of adsorbed water on dust grains, and/or (3) heating of the atmosphere followed by adiabatic cooling and condensation. In the first two cases the rapid warming of the surface would drive water/water-ice into a vapor phase and the relatively cooler atmospheric temperatures would facilitate the formation of near surface ice fog. Areas of surface dust would necessarily be cooler at night (trapping water) and warmer during the day (releasing water), relative to adjacent rockier areas. In the third case daytime high temperatures that would coincide with areas of low thermal inertia would promote heating of the atmosphere and rising motions resulting in adiabatic cooling and water ice condensation at high altitudes.

[53] One of the spectral end-members routinely identified in the TES emissivity data with the data-derived end-member methodology [*Martínez-Alonso et al.*, 2005; this study] corresponds to noise consistent with an instrument anomaly which increased gradually through TES operation [*Bandfield*, 2002]. In order to avoid the effects of this noise, TES spectral data acquired after orbit 7000 are routinely avoided in most studies. To date, more than half of the single-scan spectral data and most of the double-scan spectral data were acquired past that orbit; this portion of the TES data set is not redundant but rather critical to achieving full spectroscopic coverage of the planet. As estimated in the analysis of the Amazonis Planitia data set, approximately 85% of this type of noisy spectra were indeed acquired after orbit 7000. However, the same analysis indicated that only 31% of the spectral data acquired after orbit 7000 is dominated by this type of noise. Our results indicate that, while some noise may be present in the remaining data, this is a minor component in the emissivity measured, and surface composition can still be recognized in them.

[54] Compositional determination using the techniques described here is in general agreement with deconvolution results of atmospherically corrected TES data, as shown by deconvolution of selected TES spectra reported above and by comparison to available spectral deconvolution mineral maps at 0.25 × 0.25 degree resolution [*Bandfield*, 2002].

[55] Spectral deconvolution maps of Amazonis Planitia indicate this region is largely dominated by surface dust. The only minerals found above the detection limit were plagioclase, high-Ca pyroxene, hematite, and phyllosilicates/high-Si glass, very scarce and without overlap among them or an obvious spatial organization, except for one single pixel, corresponding to Pettit Crater, where plagioclase and high-Ca pyroxene (the main constituents of surface type 1), were identified. This is in agreement with our data-derived end-member methodology results, which identified occurrences of surface type 1 materials in Pettit Crater as well as in another unnamed crater centered at 15.47°N, 178.39°W.

[56] Spectral deconvolution results available for the Nili Fossae study area [*Bandfield*, 2002] coincide roughly with our data-derived end-members analysis in the assignment and spatial distribution of surface type 1, surface dust, and olivine. However, after thorough reexamination of the data, we conclude that the areal coverage of the surface type 1 unit was strongly overestimated by deconvolution, while that of the olivine unit was underestimated. Our results do not support other deconvolution results, such as carbonates in the olivine-rich area, or hematite and sulfates through the region. No surface type 2 was identified by deconvolution.

[57] The spectral deconvolution maps available for Mare Tyrrhenum [*Bandfield*, 2002] depict three main surface units, the first two of which coincide both in terms of spatial distribution and interpretation with our data-derived dust and surface type 1 end-members. The third one, roughly spatially corresponding to our ‘‘undetermined’’ unit, is interpreted by *Bandfield* [2002] as surface type 1 with elevated amounts of plagioclase and high-Ca pyroxene. Our observations indicate that the available plagioclase and high-Ca pyroxene library spectra do not match satisfactorily the ‘‘undetermined’’ spectra, which are most consistent with fayalite. Deconvolution assigns to this unit higher proportions of most of the other canonical TES spectral end-members (quartz, low Ca-pyroxene, hematite, sulfates, carbonates, and phylosilicates/high-Si glass), although all of them below detection limit, maybe indicating an overall inferior fit. The deconvolution RMS error for this unit, though, is only marginally larger (3%) than that for the whole study area.

5. Summary and Conclusions

[58] The SVI analysis provides a complementary view of surface spectral properties, depicting the degree of diversity of exposed materials. Its global results have remarkable spatial coherence and are broadly similar to other surface properties, such as albedo, thermal inertia, and low-resolution surface mineral maps generated with the deconvolution technique. The degree of spectral diversity determined with the SVI method is also in strong agreement with ground truth data acquired by the Martian landers. The SVI technique allows for the identification of areas of high spectral variance, indicative of larger than average surface materials diversity. Some of the high SVI regions coincide with previously known regions of large mineralogical/lithological diversity (e.g., Nili Fos-

sae, Ganges Chaos, Sinus Meridiani); others had not been previously reported (e.g., Mare Tyrrhenum).

[59] The results of our analysis indicate that the SVI is driven by surface emissivity and not by atmospheric effects. Global SVI maps obtained from the same TES data set for three spectral ranges affected by different atmospheric components show the same overall spatial distribution of high and low SVI values, and no significant correlation with the variability of those atmospheric components. Although very similar in their general trends, the three SVI maps differ locally in some instances; such differences may be indicative of their complementarity, reflecting the presence of materials with distinct characteristic features in each of the spectral ranges analyzed.

[60] Initial results from the thermophysical, spectroscopic, and morphologic analysis of three regions selected according to their SVI values have been presented. The Amazonis Planitia study area, representative of low SVI regions, is largely dominated by dust deposits, which are at TES resolution spectrally bland, presenting also very small outcrops of surface type 1 materials (basaltic composition), atmospheric water-ice, and instrument noise.

[61] The high SVI values at Nili Fossae are accounted for by the presence in this region of surface type 1 materials, surface type 2 materials, forsteritic olivine, materials most consistent with the spectral signature of phyllosilicates and/or high-Si glass, atmospheric water-ice, surface dust, and instrument noise. The olivine in Nili Fossae occurs within a distinct unit with characteristics (high thermal inertia, rough surface morphology, low albedo, layering) consistent with those of volcano-sedimentary materials. High-resolution imagery shows this is a post-Isidis impact unit overlaid by younger volcanic flows that also occupy the floor of the fossae in the region and may have been extruded along the same. Higher spatial resolution spectroscopic data of regions consistent with phyllosilicates/high-Si glass would be highly desirable to constrain their composition, and understand their geological significance.

[62] The spectral diversity of Mare Tyrrhenum, another high SVI region, can be explained by the presence of surface type 1 materials, an ‘‘undetermined’’ unit, surface dust, atmospheric water-ice, instrument noise, and (tentatively) surface type 2 materials. We interpret the ‘‘undetermined’’ unit as most consistent with fayalitic olivine in volcanic materials. High-Ca clinopyroxene library spectra are other close matches; however, their relative band depths differ substantially from those observed in the TES data. It is well known that grain size as well as packing influence spectral band depths [*Salisbury et al.*, 1991]; public spectral libraries covering the TES range and including full suites of separate grain sizes and packing modes would allow for a more definitive spectral assignment in this case.

[63] In both Nili Fossae and Mare Tyrrhenum the spectral end-members interpreted as atmospheric water-ice were found mostly constrained to surface dust/duricrust regions. We suggest possible mechanisms to explain this spatial relationship: daytime sublimation of nighttime frosts, desorption of adsorbed water on dust grains, and atmospheric heating followed by adiabatic cooling and condensation. The second mechanism would be conducive to the mobilization and deposition of salts, a potential mechanism for duricrust formation.

[64] The data-derived end-member methodology utilized in this study allows for the separation of instrument noise of unclear origin [*Bandfield*, 2002] from valid data dominated by surface emissivity, making possible the utilization of spectral data acquired past orbit 7000. This methodology can also detect very small occurrences (<0.1% of the total surface analyzed) of spectrally distinct materials.

[65] Those results demonstrate that (1) the SVI method identifies regions of surface materials diversity at TES scale, (2) surface composition mapping from TES data can be successfully achieved utilizing the methodology described here, and (3) the extraction of spectral end-members from the TES data themselves allows for the detection of spectrally distinct materials that occupy very small fractions of the total surface analyzed, equivalent to a few TES spectra. Future analysis of the spectral, thermophysical, and morphological properties of the high SVI regions identified in this study utilizing high-resolution data should contribute to the clarification of their geological significance.

[66] **Acknowledgments.** We thank Mike Smith for providing atmospheric water vapor abundance maps in digital form and Josh Bandfield for facilitating spectral deconvolution results of selected TES spectra and helpful discussions. Our appreciation to the science and operations teams responsible for the success of the Mars Global Surveyor and Mars Odyssey missions. We thank Gretchen Benedix and Ted Roush for constructive reviews. This research was supported by a National Research Council Postdoctoral Fellowship awarded to S.M.A. through the NASA Astrobiology Institute; funding was also provided by the Mars Odyssey project through a subcontract from Arizona State University.

References

Aharonson, O., M. T. Zuber, G. A. Neumann, and J. W. Head III (1998), Mars: Northern hemisphere slopes and slope distributions, *Geophys. Res. Lett.*, *25*, 4413–4416.

Altieri, F., and G. Bellucci (2003), Mars: Mapping surface units by means of statistical analysis of TES spectra, *Astron. Astrophys.*, *402*, 373–381.

Arvidson, R. E., J. L. Gooding, and H. J. Moore (1989), The martian surface as imaged, sampled, and analyzed by the Viking landers, *Rev. Geophys.*, *27*, 39–60.

Bandfield, J. L. (2002), Global mineral distributions on Mars, *J. Geophys. Res.*, *107*(E6), 5042, doi:10.1029/2001JE001510.

Bandfield, J. L. (2003), Martian global surface mineralogy from the thermal emission spectrometer: Surface emissivity, mineral map, and spectral endmember data products, in *Sixth International Conference on Mars*, *Lunar and Planet. Inst.*, Abstract 3052.

Bandfield, J. L., and M. D. Smith (2003), Multiple emission angle surface-atmosphere separations of Thermal Emission Spectrometer data, *Icarus*, *161*, 47–65.

Bandfield, J. L., V. E. Hamilton, and P. R. Christensen (2000), A global view of martian surface composition from MGS-TES, *Science*, *287*, 1626–1630.

Bandfield, J. L., T. D. Glotch, and P. R. Christensen (2003), Spectroscopic identification of carbonates in the Martian dust, *Proc. Lunar Planet. Sci. Conf. 34th*, Abstract 1723.

Bell, J. F., III, et al. (2000), Mineralogic and compositional properties of Martian soil and dust: Results from Mars Pathfinder, *J. Geophys. Res.*, *105*, 1721–1755.

Bibring, J. P., et al. (2005), Mars surface diversity as revealed by the OMEGA/Mars Express observations, *Science*, *307*, 1576–1581.

Boardman, J. W., and R. O. Green (2000), Exploring the spectral variability of the Earth as measured by AVIRIS in 1999, Proceedings of the Ninth JPL Airborne Earth Science Workshop, *JPL Publ.*, *00–18*, 55–64.

Boardman, J. W., and F. A. Kruse (1994), Automated spectral analysis: A geologic example using AVIRIS data, north Grapevine Mountains, Nevada, in *Proceedings 10th Thematic Conference on Geologic Remote Sensing*, pp. 407–418, Environ. Res. Inst. of Mich., Ann Arbor, Mich.

Boardman, J. W., F. A. Kruse, and R. O. Green (1995), Mapping target signatures via partial unmixing of AVIRIS data, Summaries 5th Annual JPL Airborne Earth Science Workshop, *JPL Publ.*, *95–1*(1), 23–26.

Christensen, P. R., et al. (1992), Thermal Emission Spectrometer experiment: Mars Observer Mission, *J. Geophys. Res.*, *97*(E5), 7719–7734.

Christensen, P. R., et al. (2000a), Detection of crystalline hematite mineralization on Mars by the Thermal Emission Spectrometer: Evidence for near-surface water, *J. Geophys. Res.*, *105*, 9623–9642.

Christensen, P. R., J. L. Bandfield, M. D. Smith, V. E. Hamilton, and R. N. Clark (2000b), Identification of a basaltic component on the Martian surface from Thermal Emission Spectrometer data, *J. Geophys. Res.*, *105*(E4), 9609–9621.

Christensen, P. R., J. L. Bandfield, V. E. Hamilton, D. A. Howard, M. D. Lane, J. L. Piatek, S. W. Ruff, and W. L. Stefanov (2000c), A thermal emission spectral library of rock-forming minerals, *J. Geophys. Res.*, *105*(E4), 9735–9739.

Christensen, P. R., R. V. Morris, M. D. Lane, J. L. Bandfield, and M. C. Malin (2001a), Global mapping of martian hematite mineral deposits: Remnants of water-driven processes on early Mars, *J. Geophys. Res.*, *106*(E10), 23,873–23,885.

Christensen, P. R., et al. (2001b), Mars Global Surveyor Thermal Emission Spectrometer experiment: Investigation description and surface science results, *J. Geophys. Res.*, *106*(E10), 23,823–23,871.

Christensen, P. R., et al. (2003), Morphology and composition of the surface of Mars: Mars Odyssey THEMIS results, *Science*, *300*, 2056–2061.

Christensen, P. R., et al. (2004), The Thermal Emission Imaging System (THEMIS) for the Mars 2001 Odyssey mission, *Space Sci. Rev.*, *118*, 85–130.

Clancy, R. T., B. J. Sandor, M. J. Wolff, P. R. Christensen, M. D. Smith, J. C. Pearl, B. J. Conrath, and R. J. Wilson (2000), An intercomparison of ground-based millimeter, MGS TES, and Viking atmospheric temperature measurements: Seasonal and interannual variability of temperatures and dust loading in the global Mars atmosphere, *J. Geophys. Res.*, *105*(E4), 9553–9572.

Clark, R. N., G. A. Swayze, K. E. Livo, R. F. Kokaly, S. J. Sutley, J. B. Dalton, R. R. McDougal, and C. A. Gent (2003), Imaging spectroscopy: Earth and planetary remote sensing with the USGS Tetracorder and expert systems, *J. Geophys. Res.*, *108*(E12), 5131, doi:10.1029/2002JE001847.

Fuller, E. R., and J. W. Head III (2002), Amazonis Planitia: The role of geologically recent volcanism and sedimentation in the formation of the smoothest plains on Mars, *J. Geophys. Res.*, *107*(E10), 5081, doi:10.1029/2002JE001842.

Golombek, M. P., et al. (1997), Overview of the Mars Pathfinder Mission and assessment of landing site predictions, *Science*, *278*, 1743–1748.

Goody, R., R. West, L. Chen, and D. Crisp (1989), The correlated-k method for radiation calculations in non-homogenous atmospheres, *J. Quant. Spectrosc. Radiat. Transfer*, *42*, 539–550.

Greeley, R., and J. E. Guest (1987), Geologic map of the eastern equatorial region of Mars, *Map I-1802–B 1:15,000,000*, U.S. Geol. Surv., Reston, Va.

Green, A. A., M. Berman, P. Switzer, and M. D. P. Craig (1988), A transformation for ordering multispectral data in terms of image quality with implications for noise removal, *IEEE Trans. Geosci. Remote Sen.*, *26*, 65–74.

Green, R. O., and J. W. Boardman (2000), Exploration of the relationship between information content and signal-to-noise ratio and spatial resolution in AVIRIS spectral data, Proceedings of the Ninth JPL Airborne Earth Science Workshop, *JPL Publ.*, *00–18*, 195–206.

Hamilton, V. E., P. R. Christensen, H. Y. McSween, R. N. Clark, and T. M. Hoefen (2001), Spectral variations in MGS-TES data of Nili Fossae: A possible source region for SNC meteorites on Mars?, *Proc. Lunar Planet. Sci. Conf. 32nd*, Abstract 2184.

Hamilton, V. E., P. R. Christensen, H. Y. McSween, and J. L. Bandfield (2003), Searching for the source regions of Martian meteorites using MGS-TES: Integrating Martian meteorites into the global distribution of igneous materials on mars, *Meteorit. Planet. Sci.*, *38*, 871–885.

Head, J. W., J. F. Mustard, M. A. Kreslavsky, R. E. Milliken, and D. R. Marchant (2003), Recent ice ages on Mars, *Nature*, *426*, 797–802.

Hoefen, T. M., and R. N. Clark (2001), Compositional variability of Martian olivines using Mars Global Surveyor Thermal Emission Spectra, *Proc. Lunar Planet. Sci. Conf. 32nd*, Abstract 2049.

Hoefen, T. M., R. N. Clark, J. C. Pearl, and M. D. Smith (2000), Unique spectral features in Mars Global Surveyor Thermal Emission Spectra: Implications for surface mineralogy in Nili Fossae, paper presented at Pasadena Meeting, Div. for Planet. Sci. of the Am. Astron. Soc., Pasadena, Calif.

Hoefen, T. M., R. N. Clark, J. L. Bandfield, M. D. Smith, J. C. Pearl, and P. R. Christensen (2003), Discovery of olivine in the Nili Fossae region of Mars, *Science*, *302*, 627–630.

Husson, N., B. Bonnet, N. A. Scott, and A. Chédin (1992), Management and study of spectroscopic information: The GEISA program, *J. Quant. Spectrosc. Radiat. Transfer*, *48*, 509–518.

Husson, N., B. Bonnet, A. Chédin, N. A. Scott, A. A. Chursin, V. F. Golovko, and V. G. Tyuterev (1994), The GEISA data bank in 1993. A PC/AT compatible computers new version, *J. Quant. Spectrosc. Radiat. Transfer*, *52*, 425–438.

Jakosky, B. M. (1986), On the thermal properties of martian fines, *Icarus*, *66*, 117–124.

Jet Propulsion Laboratory (2000), ASTER Spectral Library, Calif. Inst. of Technol., Pasadena.

Keszthelyi, L., A. S. McEwen, and T. Thorndarson (2000), Terrestrial analogs and thermal models for martian flood lavas, *J. Geophys. Res.*, *105*, 15,027–15,049.

Kieffer, H. H., S. C. Chase, E. Miner, G. Munch, and G. Neugebauer (1973), Preliminary report on infrared radiometric measurements from the Mariner 9 spacecraft, *J. Geophys. Res.*, *78*, 4291–4312.

King, E. A. (1978), Geologic map of the Mare Tyrrhenum quadrangle of Mars, *Map I-1073*, 1:5,000,000, U.S. Geol. Surv., Reston, Va.

Kruse, F. A., A. B. Lefkoff, J. W. Boardman, K. B. Heidebrecht, A. T. Shapiro, P. J. Barloom, and A. F. H. Goetz (1993), The spectral image processing system (SIPS)–Interactive visualization and analysis of imaging spectrometer data, *Remote Sens. Environ.*, *44*, 145–163.

Malin, M. C., G. E. Danielson, A. P. Ingersoll, H. Masursky, J. Veverka, M. A. Ravine, and T. A. Soulanille (1992), Mars-Observer Camera, *J. Geophys. Res.*, *97*(E5), 7699–7718.

Mangold, N., S. Maurice, W. C. Feldman, F. Costard, and F. Forget (2004), Spatial relationships between patterned ground and ground ice detected by the Neutron Spectrometer on Mars, *J. Geophys. Res.*, *109*, E08001, doi:10.1029/2004JE002235.

Martínez-Alonso, S. (2002), Mineralogical mapping of Mars using data-derived endmembers, paper presented at Astrobiology Science Conference 2002, NASA Ames Res. Cent., Moffit Field, Calif.

Martínez-Alonso, S., B. C. Kindel, and M. T. Mellon (2002), Analysis of areas of high spectral variance detected in TES data, paper presented at NASA Astrobiology Institute General Meeting, Ariz. State Univ., Tempe, Ariz.

Martínez-Alonso, S., B. C. Kindel, M. T. Mellon, and B. M. Jakosky (2003), Spectral variance derived from MGS-TES data as a tool to detect hydrothermal systems, *Proc. Lunar Planet. Sci. Conf. 34th*, Abstract 1805.

Martínez-Alonso, S., B. M. Jakosky, M. T. Mellon, and N. E. Putzig (2005), A volcanic interpretation of Gusev Crater surface materials from thermophysical, spectral, and morphological evidence, *J. Geophys. Res.*, *110*, E01003, doi:10.1029/2004JE002327.

McSween, H. Y., et al. (2004), Basaltic rocks analyzed by the Spirit Rover in Gusev Crater, *Science*, *305*, 842–845.

Mellon, M. T., and B. M. Jakosky (1995), The distribution and behavior of Martian ground ice during past and present epochs, *J. Geophys. Res.*, *100*, 11,781–11,799.

Mellon, M. T., B. M. Jakosky, H. H. Kieffer, and P. R. Christensen (2000), High-resolution thermal inertia mapping from the Mars Global Surveyor Thermal Emission Spectrometer, *Icarus*, *148*, 437–455.

Mellon, M. T., W. C. Feldman, and T. H. Prettyman (2004), The presence and stability of ground ice in the southern hemisphere of Mars, *Icarus*, *169*, 324–340.

Mustard, J. F., C. D. Cooper, and M. K. Rifkin (2001), Evidence for recent climate change on Mars from the identification of youthful near-surface ground ice, *Nature*, *412*, 411–414.

Pearl, J. C., M. D. Smith, B. J. Conrath, J. L. Bandfield, and P. R. Christensen (2001), Observations of martian ice clouds by the Mars Global Surveyor Thermal Emission Spectrometer: The first martian year, *J. Geophys. Res.*, *106*(E10), 12,325–12,338.

Pelkey, S. M., and B. M. Jakosky (2002), Surficial geologic surveys of Gale Crater and Melas Chasma, Mars: Integration of remote-sensing data, *Icarus*, *160*, 228–257.

Pelkey, S. M., B. M. Jakosky, and M. T. Mellon (2001), Thermal inertia of crater-related wind-streaks on Mars, *J. Geophys. Res.*, *106*(E10), 23,909–23,920.

Peterfreund, A. R. (1981), Visual and infrared observations of wind streaks on Mars, *Icarus*, *45*, 447–467.

Plescia, J. B. (1990), Recent flood lavas in the Elysium Region of Mars, *Icarus*, *88*, 465–490.

Presley, M. A., and P. R. Christensen (1997), Thermal conductivity measurements of particulate materials. 2. Results, *J. Geophys. Res.*, *102*(E3), 6551–6566.

Press, W. H., B. P. Flannery, S. A. Teukolsky, and W. T. Vetterling (1992), *Numerical Recipes in C: The Art of Scientific Computing*, 2nd ed., Cambridge Univ. Press, New York.

Putzig, N. E., M. T. Mellon, K. A. Kretke, and R. E. Arvidson (2005), Global thermal inertia and surface properties of Mars from the MGS mapping mission, *Icarus*, *173*, 325–341.

Rieder, R., T. Economou, H. Wänke, A. Turkevich, J. Crisp, J. Brückner, G. Dreibus, and H. Y. McSween Jr. (1997), The chemical composition of Martian soil and rocks returned by the Mobile Alpha Proton X-ray Spectrometer: Preliminary results from the X-ray mode, *Science*, *278*, 1771–1774.

Rogers, D., and P. R. Christensen (2003), Age relationship of basaltic and andesitic surface compositions on Mars: Analysis of high-resolution TES observations of the northern hemisphere, *J. Geophys. Res.*, *108*(E4), 5030, doi:10.1029/2002JE001913.

Ruff, S. W., and P. R. Christensen (2003), Identifying compositional heterogeneity in Mars' Nili Patera Caldera using THEMIS and TES data, *Proc. Lunar Planet. Sci. Conf. 34th*, Abstract 2068.

Salisbury, J. W., L. S. Walter, N. Vergo, D. M. D'Aria (1991), *Infrared (2. 1–25 μm) Spectra of Minerals*, 267 pp., Johns Hopkins Univ. Press, Baltimore, Md.

Scott, D. H., and M. G. Chapman (1991), Mars Elysium Basin: Geologic/volumetric analyses of a young lake and exobiologic implications, *Proc. Lunar Planet. Sci. Conf 21st*, *XXI*, 669–677.

Seidelmann, P. K., et al. (2002), Report of the IAU/IAG working group on cartographic coordinates and rotational elements of the planets and satellites: 2000, *Celestial Mech. Dyn. Astron.*, *82*, 83–110.

Smith, M. D. (2002), The annual cycle of water vapor on Mars as observed by the Thermal Emission Spectrometer, *J. Geophys. Res.*, *107*(E11), 5115, doi:10.1029/2001JE001522.

Smith, M. D. (2004), Interannual variability in TES atmospheric observations of Mars during 1999–2003, *Icarus*, *167*, 148–165.

Smith, M. D., J. L. Bandfield, and P. R. Christensen (2000a), Separation of atmospheric and surface spectral features in Mars Global Surveyor Thermal Emission Spectrometer (TES) spectra, *J. Geophys. Res.*, *105*(E4), 9589–9607.

Smith, M. D., J. C. Pearl, B. J. Conrath, and P. R. Christensen (2000b), Mars Global Surveyor Thermal Emission Spectrometer (TES) observations of dust opacity during aerobraking and science phasing, *J. Geophys. Res.*, *105*(E4), 9539–9552.

Squyres, S. W., et al. (2004a), In situ evidence for an ancient aqueous environment at Meridiani Planum, Mars, *Science*, *306*, 1709–1714.

Squyres, S. W., et al. (2004b), The Spirit rover's Athena science investigation at Gusev Crater, Mars, *Science*, *305*, 794–799.

Squyres, S. W., et al. (2004c), The Opportunity Rover's Athena Science Investigation at Meridiani Planum, Mars, *Science*, *306*, 1698–1703.

Switzer, P., and A. Green (1984), Min/max autocorrelation factors for multivariate spatial imagery, *Tech. Rep. 6*, Dept. of Statistics, Stanford Univ., Stanford, Calif.

Walter, M. R., and D. J. Des Marais (1993), Preservation of biological information in thermal spring deposits: Developing a strategy for the search for fossil life on Mars, *Icarus*, *101*, 129–143.

Wänke, H., J. Brückner, G. Dreibus, R. Rieder, and I. Ryabchikov (2001), Chemical composition of rocks and soils at the Pathfinder site, *Space Sci. Rev.*, *96*, 317–330.

Wyatt, M. B., and H. Y. McSween (2002), Spectral evidence for the weathered basalt as an alternative to andesite in the northern lowlands of Mars, *Nature*, *417*, 263–266.

Zuber, M. T., D. E. Smith, S. C. Solomon, D. O. Muhleman, J. W. Head, J. B. Garvin, J. B. Abshire, and J. L. Bufton (1992), The Mars-Observer Laser Altimeter investigation, *J. Geophys. Res.*, *97*(E5), 7781–7797.

B. M. Jakosky, B. C. Kindel, and M. T. Mellon, Laboratory for Atmospheric and Space Physics, University of Colorado, Campus Box 392, Boulder, CO 80309-0392, USA.

S. Martínez-Alonso, Department of Geological Sciences, University of Colorado, Campus Box 392, Boulder, CO 80309-0392, USA. (sara.martinez-alonso@colorado.edu)